Latent Heating from TRMM Satellite Measurements

W.-K. Tao[1], E.A. Smith[1],
R. Adler[1], Z. Haddad[2], A. Hou[1], T. Iguchi[3], R. Kakar[4], T. Krishnamurti[5], C. Kummerow[6],
S. Lang[7], R. Meneghini[1], K. Nakamura[8], T. Nakazawa[9], K. Okamoto[10], W. Olson[11], S. Satoh[3],
S. Shige[10], J. Simpson[1], Y. Takayabu[12], G. Tripoli[13], and S. Yang[14]

[1] *Laboratory for Atmospheres, NASA/Goddard Space Flight Center, Greenbelt, MD 20771, USA*

[2] *NASA/Jet Propulsion Laboratory-California Inst. of Technology, Pasadena, CA 91109, USA*

[3] *National Institute of Information & Communications Technology, Tokyo 184-8795, JAPAN*

[4] *NASA/Headquarters, Washington, DC 20546, USA*

[5] *Dept. of Meteorology, Florida State Univ., Tallahassee, FL 32306, USA*

[6] *Dept. Of Atmospheric Science, Colorado State Univ., Fort Collins, CO 80523, USA*

[7] *Science Systems and Applications Inc., Greenbelt, MD 20706, USA*
[Mail Code 912, NASA/Goddard Space Flight Center, Greenbelt, MD 20771, USA]

[8] *Hydrospheric Atmospheric Research Center, Nagoya Univ., Nagoya 464-8601, JAPAN*

[9] *Japan Meteorological Agency-Meteorological Research Institute, Tsukuba 305-0052, JAPAN*

[10] *Dept. of Aerospace Engineering, Osaka Prefecture Univ., Sakai, Osaka 599-8531, JAPAN*

[11] *UMBC/Joint Center for Earth Systems Technology, Baltimore, MD 21250, USA*
[Mail Code 912, NASA/Goddard Space Flight Center, Greenbelt, MD 20771, USA]

[12] *Center for Climate System Research, Univ. of Tokyo, Tokyo 153-8904, JAPAN*

[13] *Dept. of Atmospheric & Oceanic Sciences, Univ. of Wisconsin, Madison, WI 53706, USA*

[14] *School of Computational Sciences, George Mason Univ., Fairfax, VA 22030, USA*
[Mail Code 912.1, NASA/Goddard Space Flight Center, Greenbelt, MD 20771, USA]

Submitted to
Bulletin of the American Meteorological Society

November 2004

Corresponding Author Contact Information:
Dr. Wei-Kuo Tao
Mesoscale Atmospheric Processes Branch, Code 912
NASA/Goddard Space Flight Center
Greenbelt, MD 20771
(301) 614-6269; tao@agnes.gsfc.nasa.gov

Popular Summary

Latent Heating from TRMM Satellite Measurements

W.-K. Tao, E.A. Smith,
R. Adler, Z. Haddad, A. Hou, T. Iguchi, R. Kakar, T. Krishnamurti, C. Kummerow,
S. Lang, R. Meneghini, K. Nakamura, T. Nakazawa, K. Okamoto, W. Olson, S. Satoh,
S. Shige, J. Simpson, Y. Takayabu, G. Tripoli, and S. Yang

Submitted to *Bulletin of the American Meteorological Society*

Rainfall production is the key ingredient of the Earth's hydrological cycle, the main driver of atmospheric and surface water and energy budgets, and the primary diabatic heat source within the atmosphere via latent heat release. Fundamentally, latent heat release is a consequence of phase changes between the vapor, liquid, and solid forms of water, processes which occur spatially and temporally heterogeneously over a precipitating storm's lifecycle. The temporally averaged horizontal pattern of latent heating is a major determinant of the Earth's general circulation, while the vertical distribution directly modulates large-scale meridional and zonal circulations, particularly in the tropics. Moreover, the spatial distribution of latent heating exerts significant influence on energetic efficiencies of baroclinic mid-latitude weather systems.

The Tropical Rainfall Measuring Mission (TRMM) is providing the first comprehensive global scale climatology of rainfall over the tropics and sub-tropics. These four-dimensional data sets are now being used to estimate the associated space-time latent heating structures. Such distributions of rainfall and inferred latent heating will ultimately be used to advance an understanding of the global water and energy cycle, and aid in improved predictions of weather and climate. This study describes a set of retrieval algorithms being used for estimating latent heating from TRMM observations and their consequent applications for the aforementioned purposes. The nature of these algorithms and some of the main characteristics of their resultant heating products are described. The issue of validation of the heating products is also examined. The study concludes with an overview of how latent heating estimates are being used in conjunction with global weather and climate models, and remarks intended to stimulate further research concerning the topic of satellite-based latent heating retrieval.

Abstract

Rainfall production is the fundamental variable within the Earth's hydrological cycle because it is both the principal forcing term in surface water budgets and its energetics corollary, latent heating, is the principal source of atmospheric diabatic heating. Latent heat release itself is a consequence of phase changes between the vapor, liquid, and frozen states of water. The properties of the vertical distribution of latent heat release modulate large-scale meridional and zonal circulations within the tropics -- as well as modifying the energetic efficiencies of mid-latitude weather systems. This paper focuses on the retrieval of latent heat release from satellite measurements generated by the Tropical Rainfall Measuring Mission (TRMM) satellite observatory, which was launched in November 1997 as a joint American-Japanese space endeavor. Since then, TRMM measurements have been providing an accurate four-dimensional account of rainfall over the global tropics and sub-tropics, information which can be used to estimate the space-time structure of latent heating across the Earth's low latitudes.

The paper examines how the observed TRMM distribution of rainfall has advanced an understanding of the global water and energy cycle and its consequent relationship to the atmospheric general circulation and climate via latent heat release. A set of algorithm methodologies that are being used to estimate latent heating based on rain rate retrievals from the TRMM observations are described. The characteristics of these algorithms and the latent heating products that can be generated from them are also described, along with validation analyses of the heating products themselves. Finally, the investigation provides an overview of how TRMM-derived latent heating information is currently being used in conjunction with global weather and climate models, concluding with remarks intended to stimulate further research on latent heating retrieval from satellites.

1. Introduction

The global hydrological cycle with its underlying precipitation controls helps determine the behavior of the Earth's weather and climate systems and is central to understanding their variability. Some two-thirds of global rainfall occurs over the tropics [1], where it has a profound effect on the general circulation of the atmosphere because rainfall's energetic equivalent, latent heating, is the tropical convective heat engine's primary fuel source; Riehl and Malkus (1958). At low latitudes, latent heating stemming from extended bands of rainfall modulates large-scale zonal and meridional circulations and their consequent mass overturnings (e.g., Hartmann *et al.* 1984; Hack and Schubert 1990). Latent heating is also the principal energy source in creation of long-lived tropical waves, their growth, vertical structure, and propagation (e.g., Puri 1987 and Lau and Chan 1988). Moreover, the distinct vertical distribution properties of convective and stratiform latent heating profiles help influence climatic outcomes via their tight control on large-scale circulations; Lau and Peng (1987), Nakazawa (1988), Sui and Lau (1988), Emanuel et al. (1994), Yanai et al. (2000), Sumi and Nakazawa (2002), and Schumacher *et al.* (2003).

The purpose of this paper is to describe how reliable latent heating profiles are derived from satellite rain rate retrievals, particularly those being made by the Tropical Rainfall Measuring Mission (TRMM) satellite. As an example, the Cover Figure provides a color depiction of averaged patterns of latent heating determined from TRMM measurements and mapped at three vertical levels (2, 5, and 8 km) for a 5-year period (1998-2002), along with the associated averaged surface rain rate map. [This diagram is discussed in detail in section 3.2.]

The TRMM satellite is the centerpiece of a joint rainfall mission between the United States' and Japanese space agencies, NASA and JAXA (previously NASDA), providing for the first time high quality 4-dimensional measurements of rainfall and the associated space-time structures of latent heating over the global tropics and sub-tropics. The TRMM observatory was launched in November 1997, in a 350-km orbit inclined 35 degrees to the Earth's equatorial plane. The primary rain measuring instruments are JAXA's Ku-band Precipitation Radar (PR) and NASA's 9-channel TRMM Microwave Imager (TMI). The papers of Okamoto et al. (1988), Simpson *et al.* (1988, 1996), Nakamura et al. (1990), Okamoto and Kozu (1993), Kummerow et al. (1998), Kozu et al. (2000), Okamoto (2003), and Smith and Hollis (2003) provide details concerning the TRMM observatory, orbit, instruments, data, rain retrieval algorithms, and validation.

---

[1] The tropics are generally defined as the area bounded by the 25°N-25°S latitude zone.

Latent heating estimation from satellite is rooted in literature associated with the first spaceborne passive microwave (PMW) rain radiometer, viz., the study by Adler and Rodgers (1977) concerning total-column latent heating within tropical cyclones. This study was based on measurements from the 19 GHz Electrically Scanning Microwave Radiometer (ESMR), an instrument flown on NASA's Nimbus-5 satellite (Wilheit *et al.* 1976). Latent heating is the portion of diabatic heating released or absorbed within the atmosphere as a result of phase changes of water (i.e., gas to liquid, liquid to solid, gas to solid, and their reverse processes) -- all requiring exchanges of heat. The coupled terms describing phase changes are condensation-evaporation, freezing-melting, and deposition-sublimation. Latent heating is dominated by phase changes between water vapor and small liquid or frozen cloud-sized particles. These processes are not directly detectable with remote sensing (or for that matter, with *in situ* measuring), which explains why the retrieval schemes to be described depend so heavily on the use of some type of cloud ensemble model (CEM), or in modern nomenclature -- cloud resolving model (CRM).

High resolution CRMs are an outgrowth of limited-area mesoscale models that use detailed physical parameterizations, particularly for atmosphere / surface radiative transfer, surface radiation-heat-moisture-momentum fluxes, boundary layer heat-moisture-momentum turbulent transports, and cloud microphysical processes -- along with grid resolutions sufficient to simulate the dynamical interactions of individual and ensemble clouds with the large-scale environment. High resolution precludes the need for CRM integrations to parameterize the dynamical heat and mass flux processes associated with clouds and their lifecycles -- as required in all current global-scale models. The studies of Soong and Tao (1980, 1984) were some of the first to experiment with CRMs, designed to understand interactions between clouds and their larger scale environment. Notably, early CRMs could credibly reproduce the statistical properties of cloud ensembles as first emphasized by Soong and Tao (1980), Lipps and Hemler (1986), Tao and Soong (1986), and Tao et al. (1987). At present, modern mesoscale models used in CRM mode (or with CRM nests) are being used to simulate phase changes of water and explicit conversion of water species in support of latent heating retrieval from satellite measurements, notably the Goddard Cumulus Ensemble (GCE) model developed by Tao and Soong (1986), Tao and Simpson (1993), and Tao *et al.* (2003a), the University of Wisconsin Nonhydrostatic Modeling System (UW-NMS) developed by Tripoli (1992a-b, 2004), and the Penn State-NCAR Mesoscale Model 5 (MM5) described by Dudhia (1993).

Under the Boussinesq approximation, the thermodynamic (or temperature) budget that can be explicitly calculated from CRMs:

$$Q_1 - Q_R = \bar{\pi}\{-(1/\bar{\rho})\,[\overline{\partial \bar{\rho} w' \theta' / \partial z}] - \overline{\nabla \bullet V'\theta'}\} + (1/c_p)\,[L_v(c-e) + L_f(f-m) + L_s(d-s)] \qquad (1)$$

where the primes indicate deviations from the large-scale environment, i.e., due to cloud processes at smaller scales. The variable θ is potential temperature, $\bar{\rho}$ is density, $\bar{\pi} = (p / P_{oo})^{R/c_p}$ is non-dimensional pressure (where p and p_{oo} are dimensional and reference pressures, respectively, with p_{oo} taken as 1000 hPa), and c_p and R are the specific heat of dry air at constant pressure and the gas constant of dry air, respectively. The variables (L_v, L_f, L_s) are the latent heats of condensation, freezing, and sublimation, respectively, while the variables (c, e, f, m, d, s) identify the rates of: condensation of cloud droplets, evaporation of cloud droplets and rain drops, freezing of water droplets and rain drops, melting of ice crystals, snow flakes, graupel and hail, deposition of ice crystals, and sublimation of all ice hydrometeors, respectively. Note that the term $(1/c_p)\,[L_v(c-e) + L_f(f-m) + L_s(d-s)]$ is defined as the latent heating (LH) due to microphysical phase changes.

The term Q_1 is referred to as the apparent heat source, stemming from the diagnostic analysis approach described in a seminal paper by Yanai *et al.* (1973), while Q_R is the radiative heating rate associated with radiative transfer processes. Note that the first two terms on the right-hand side of (1) are the vertical and horizontal eddy heat flux convergences ($\bar{\pi}[\overline{\partial w'\theta'/\partial z}]$ and $\bar{\pi}[\overline{\nabla \bullet V'\theta'}]$ for an isosteric column), where the horizontal diffusion term is neglected when (1) is spatially averaged over an area suitable for diagnostic analysis.

Figure 1 illustrates instantaneous latent heating structures associated with both a mid-latitude and a tropical mesoscale convective system (MCS) simulated by the GCE-CRM in a two-dimensional framework. The cases were drawn from two field campaigns, the mid-latitude continental PRE-STORM and tropical oceanic TOGA-COARE experiments. [2] Evident in the

---

[2] (1) PRE-STORM *(Preliminary Regional Experiment for STORM-Central)* -- which took place in Kansas and Oklahoma during May-Jun'85 (Cunning 1986), and (2) TOGA-COARE *(Tropical Ocean-Global Atmosphere -- Coupled Ocean-Atmosphere Response Experiment)* -- which took place within Pacific Ocean's warm pool from Nov'92 to Feb'93 (Webster and Lukas 1992; Nakazawa 1995).

figure are: (1) condensation heating in lower to middle troposphere at convective leading edge of cloud systems; (2) deposition heating in upper parts of convective and stratiform regions; (3) cooling at low levels in stratiform regions stemming from evaporation of rain; (4) cooling from melting of precipitation particles, mainly occurring in narrow layer near freezing level; and (5) cooling from sublimation adjacent to depositional heating in stratiform region. The alternating heating and cooling pattern at upper levels is mainly caused by gravity wave dispersion induced by deep convection. This mechanism is more significant for the mid-latitude case because its associated convective updrafts are generally stronger.

Not surprisingly, there are also major differences between the two cases. For example, cooling within the stratiform regions is larger and deeper for the mid-latitude case in comparison to the tropical case. This is due to the generally drier environment at mid-latitudes. In addition, the level separating the heating and cooling layers within the stratiform regions (indicating the melting level) is different for the two systems. The primary features of squall line structure simulated using the GCE-CRM are generally consistent with observed squall lines; see Biggerstaff and Houze (1991) and Jorgensen *et al.* (1997).

Based on a residue approach, the composite diabatic heating profile of Q_1 can be derived indirectly over a spatial domain by measuring profiles of temperature, pressure, and 3-dimensional wind vector from a suitably spaced circumscribing network of radiosondes. This is called a "diagnostic heat budget", first described by Yanai *et al.* (1973), extensively studied by others (e.g., Nitta 1977, Houze 1982, 1989, 1997; Johnson 1984), and expressed by:

$$Q_1 = \bar{\pi}\left[\frac{\partial \bar{\theta}}{\partial t} + \bar{V} \bullet \nabla \bar{\theta} + \bar{w}\frac{\partial \bar{\theta}}{\partial z}\right] \tag{2}$$

where Q_1 represents the sum of LH (i.e., from microphysical phase changes), $\bar{\pi}\left[\overline{\partial w'\theta'/\partial z}\right]$, and Q_R, while the right-hand side is the total derivative of θ (times the non-dimensional pressure) measurable from radiosonde data. There is an accompanying Q_2 equation for the apparent moisture sink (or drying), which is similar to eqn (2) except that θ is replaced by water vapor specific humidity (q) and Q_1 is replaced by $-Q_2$, i.e., the sum of net condensation/deposition and vertical eddy moisture flux convergence ($(L_v / c_p)\left[\overline{\partial w' q_v' / \partial z}\right]$).

Clearly, latent heating estimates from satellite-retrieved rain rate profiles could be assessed using Q_1 budgets determined from CRM simulations, or even from regional- to large-scale prediction models and/or global climate reanalysis products (e.g., Nigam *et al.* 2000). However, since it will be shown that the current latent heating retrieval schemes are all directly or indirectly tied to CRMs, the more independent approach in conducting satellite validation is to use the radiosonde-based diagnostic heat budget approach discussed above -- this notwithstanding inherent uncertainties in such budgets due to instrumental and sampling errors in sounding data (e.g., Mapes et al. 2003). Therefore, for purpose of this study, Q_1 budgets diagnosed from sounding observations taken during three TRMM field campaigns (SCSMEX, TRMM-LBA, and KWAJEX), as well as other past and current field campaigns (GATE, PRE-STORM, TOGA-COARE, and DOE-ARM), are used as the principal validation data sets. [3]

Figure 2 illustrates the evolution of Q_1, determined diagnostically from TOGA-COARE soundings for the period 19-27 December 1992, and accompanied by explicit calculations from the GCE-CRM for the same period. The temporal variations of the two sets of heating profiles are in reasonably close agreement. This is because the time-varying large-scale advection of temperature and moisture superimposed within the GCE model is the main forcing (Soong and Tao 1980), and the simulation is driven by observed advective tendencies from the soundings. The structures associated with all five major rainfall events are in close agreement, with the exception that the diagnostic results are smoother. This is because the diagnosed Q_1 quantities are calculated using 6-hourly soundings, after which a binomial filter is applied to the resultant time series (Lin and Johnson 1996), whereas the GCE-CRM Q_1 estimates are based on 2-minute statistics of cloud processes, with only a 30-minute running average filter applied.

---

[3] (1) SCSMEX *(South China Sea Monsoon Experiment)* -- which took place in South China Sea environs during May-Jun'98 (Lau *et al.* 2000); (2) TRMM-LBA *(TRMM Large Scale Biosphere-Atmosphere Experiment in Amazonia)* -- which took place in Rondonia, Brazil during Jan-Feb'99 (Halverson *et al.* 2002, Petersen *et al.* 2002); (3) KWAJEX (*TRMM Kwajalein Experiment)* -- which took place in vicinity of Kwajalein Atoll, Republic of Marshall Islands during Jul-Sep'99 (Yuter *et al.* 2004); (4) GATE *(Global Atmospheric Research Programme (GARP) - Atlantic Tropical Experiment)* -- which took place in eastern tropical Atlantic Ocean during Jun-Sep'74 (GATE-ISMG 1974, Houze and Betts 1981); and (5) DOE-ARM *(Department of Energy-Atmospheric Radiation Measurement)* Program -- which supports experiments in Oklahoma at DOE-ARM's Southern Great Plains-Cloud and Radiation Test Bed (SGP-CART) site (Stokes and Schwartz 1994).

Since CRMs such as GCE and UW-NMS can reproduce vertical heating structures with good fidelity for a prescribed forcing, it is possible to use simulations such as those in Fig. 2 to establish relationships between vertical hydrometeor profiles retrievable from satellite measurements and the associated LH profiles. Therefore, as will be shown, CRM simulations are now being used to relate remotely-sensed precipitation structures that are retrieved from TRMM sensor data to vertical LH profiles that cannot be directly sensed. In essence, by simulating various types of clouds and cloud systems for different geographic locations and climate regimes, relationships are created which associate cloud/precipitation hydrometeor profiles to LH profiles for different remote sensing applications; see Tao *et al.* (1990, 1993b, 2000, 2001), Smith et al. (1994a-b), Olson et al. (1999, 2004), Yang and Smith (1999a, 2000), Shige et al. (2004), and Yang (2004).

In section 2, a set of five LH algorithms developed for TRMM applications are described. Highlights from various applications of the algorithms are presented in section 3 with further results for selected validation analyses given in section 4. Section 5 is a discussion of how TRMM LH products are currently being used in conjunction with global weather and climate models. Finally, section 6 offers conclusions including remarks intended to stimulate further research.

2. Descriptions, Physical Bases, and Synthesis of Latent Heating Algorithms

In this section, five different LH profile algorithms that have been developed for application with the various TRMM rain rate retrieval products are examined. These are referred to as the Goddard Convective-Stratiform Heating algorithm (CSH), the Goddard Profiling Heating algorithm (GPROF Heating), the Hydrometeor Heating algorithm (HH), the Precipitation Radar Heating algorithm (PRH), and the Spectral Latent Heating algorithm (SLH). The CSH, GPROF, and SLH algorithms require the complete complement of cloud model data generated by a CRM. Table 1 provides a summary of the algorithms including their principal authorship, the main algorithm inputs, identification of data sets to which they have been applied, and the notional space-time resolutions associated with the algorithms. To aid in understanding these algorithms and in the interpretation of their results given in sections 3-5, a compilation of their general strengths and weakness are given in Table 2.

The application of the various algorithms to TRMM precipitation data sets is not completely general. For example, as currently implemented the PRH and SLH algorithms

confine themselves only to PR-generated rain rate retrievals. The PR rain retrieval scheme is referred to as TRMM standard algorithm 2a25, a level-2 rain rate profile algorithm in which level-2 signifies that it produces results on an instantaneous time-basis and at the full ground resolution associated with a given radar beam. [Note that a level-3 algorithm produces monthly-averaged rain rates over a 5-degree grid mesh.] The PR rain profile algorithm is coupled to another level-2 algorithm that denotes whether a given rain rate profile represents convective or stratiform rainfall conditions (TRMM standard algorithm 2a23). [The papers of Iguchi *et al.* (2000) and Meneghini *et al.* (2000) describe the methodology of the level-2 PR algorithms.]

Alternatively, the GPROF Heating algorithm is strictly configured for applications directly to TMI radiance data, as part of the TMI level-2 precipitation algorithm, referred to as the TRMM standard algorithm 2a12. The TMI level-2 algorithm produces density profiles of precipitating liquid and ice hydrometeors, suspended liquid and ice hydrometeors, latent heating, and surface rain rates -- as well as an estimate of the convective fraction of rain. Because the TMI radiometer swath width is three times that of the PR radar (i.e., wide swath versus narrow swath), the spatial duty cycle of the GPROF Heating algorithm is three times that of the PRH and SLH algorithms. On the other hand, because the effective ground resolution of the TMI retrievals is lower than that of the PR, the GPROF Heating algorithm retrievals lack the sharpness and detail of PR-based retrievals. [The papers of Kummerow *et al.* (1996, 2001) and Olson *et al.* (1999, 2004) describe the methodology of the level-2 TMI precipitation algorithm.]

The CSH and HH algorithms are not restricted to applications with any particular TRMM rainfall algorithm -- with the constraint that the CSH algorithm requires explicit information concerning whether a given rain profile is convective or stratiform in nature. Both of these algorithms can be applied to rain profiles from the level-2 PR or TMI algorithms, or to rain profiles from the level 2 Combined PR-TMI retrieval algorithm referred to as TRMM standard algorithm 2b31 (also a narrow swath algorithm because it requires PR data). [The papers of Haddad *et al.* (1997) and Smith *et al.* (1997) describe the methodology of the level-2 Combined PR-TMI algorithm.] Moreover, the HH algorithm can be used with rain profile products derived from any other type of satellite or radar platform. The CSH algorithm requires information on surface rain rate, the fractions of convective and stratiform precipitation, and a geographic locater/storm type flag (pointing to pre-calculated LH profiles contained in look-up tables),

whereas the HH algorithm requires vertical profiles of precipitation mass fluxes (either or both liquid and frozen phases), which are directly proportional to rain rates.

2.1 CSH algorithm

Diagnostic budget studies (e.g., Houze 1982 and Johnson 1984) and cloud modeling studies (see review by Tao 2003) have shown that the characteristic LH vertical profile in the anvil region of tropical MCSs is considerably different than the characteristic LH vertical profile in the convective region. Generally, for both observed and simulated convective systems, evaporative cooling in the lower troposphere below a bow-shape positive heating profile for the remaining upper cloud layers (peaking in the upper troposphere), is the dominant feature within a stratiform precipitation region (the archetypal, S-shape curve stratiform LH profile), while a combination of vertically continuous condensation and deposition heating (peaking in the middle troposphere) is the dominant feature for the convective rain stage (forming the archetypal, deep, all-positive, bow-shape curve convective LH profile). Based on these findings, the convective-stratiform heating (CSH) algorithm was developed -- described by Tao *et al.* (1993b), with additional references concerning its applications summarized in Table 1.

The CSH algorithm is designed for computational efficiency and robustness in that it uses pre-calculated information on the physical relationships between rainfall and latent heating, cannot generate pathological estimates, and is applicable to input from any level-2 (or level-3) TRMM rain profile algorithm. It relies on the principle that under steady-state conditions, surface precipitation is equivalent to the vertically integrated net condensation/deposition in the atmosphere. The foundations of the algorithm are pre-calculated look-up tables associated with convective and stratiform Q_1 profiles, generated primarily from GCE-CRM simulations that have been normalized by surface rain rate. In addition to the model calculations, observations drawn from the diagnostic studies of Yanai *et al.* (1973), Houze and Rappaport (1984), Johnson (1984), Houze (1989), Chong and Hauser (1990), and Gallus and Johnson (1991) are used to enhance the variance properties of the initial Q_1 profiles in the look-up tables. Normalized convective and stratiform Q_1 profiles, appropriate for an observed region and cloud type, are selected from the look-up tables, scaled by the TRMM-retrieved convective and stratiform rain fractions, then combined to yield the total Q_1 profile. Emphasis has been given to ensuring that the vertical structures of the retrieved Q_1 profiles are physically consistent with those found from

diagnostic budget studies. Therefore, it can be anticipated that some level of disagreement will arise between the CSH algorithm and various other algorithms not so constrained.

The implementation of CSH described here employs surface convective / stratiform rain rates derived from the PR algorithm, applied on time scales ranging from 3 hours to 1 month and space scales ranging from 50 to 500 km. A distinguishing feature of the CSH algorithm is that it has been used extensively for regions and time periods associated with a number of field programs for which diagnostic-based Q_1 profiles are available for comparison and contrast with reconstructed and retrieved profiles. To date, field program data that have been examined in conjunction with the CSH algorithm include: (1) GATE, (2) EMEX [4], (3) PRE-STORM, (4) TOGA-COARE, (5) SCSMEX, (6) TRMM-LBA, (7) KWAJEX, and (8) DOE-ARM.

2.2 GPROF Heating algorithm

The GPROF Heating algorithm is designed specifically for applications with TMI PMW radiance observations. A large database of explicitly related hydrometeor and Q_1-Q_R profiles generated by GCE-CRM and MM5-CRM simulations is pre-calculated, along with PMW radiances calculated using a radiative transfer model (the combined result is called a cloud-radiation data base). Thus, given a set of TMI-measured radiances, the look-up table is scanned to identify those profiles exhibiting radiative characteristics consistent with the observations. The radiatively consistent profiles are then composited using a Bayesian approach to retrieve a best estimate of the hydrometeor and heating profiles.

Originally developed for applications to SSM/I data, the Bayesian method has been adapted for applications to TMI radiance data, and it is effectively integrated with the GPROF TMI precipitation retrieval algorithm (see Olson *et al.* 1999, 2004). Versions of GPROF have been used by Rodgers et al. (1998, 2000) to diagnose latent heating distributions in Hurricane Opal and Supertyphoon Paka, to study the relationships between heating and storm intensification. Recently Yang *et al.* (2004) demonstrated that vertical profiles of GPROF latent heating were fairly consistent with independent estimates derived from Kwajalein dual-Doppler radar data and SCSMEX rawinsonde analyses

2.3 HH algorithm

---

[4] EMEX *(Equatorial Monsoon Experiment)* -- which took place in ocean tropics north of Australia during Jan-Feb'87 (Webster and Houze 1991).

Without reference to pre-calculated LH profiles in look-up tables, it is possible to treat each layer of the atmosphere independently, estimating the net flux of water mass in or out of the layers and assuming under steady-state conditions, that the fluxes are compensated by some local decrease (increase) of hydrometeors by microphysical processes. A decrease is thus associated with evaporation, melting, or sublimation cooling, whereas an increase is associated with condensation, freezing, or deposition heating -- and thus the basis for a hydrometeor mass flux heating algorithm. The first application of a LH algorithm applied to actual satellite-retrieved hydrometeor profiles was a HH scheme -- performed by Smith *et al.* (1992) on Pacific Supertyphoon Thelma, using Special Sensor Microwave Imager (SSM/I) measurements from a Defense Military Satellite Program (DMSP) satellite. Based on a different HH algorithm formulated by Tao *et al.* (1990), Tao *et al.* (1993b) used the Thelma hydrometeor retrievals to produce an alternate set of LH profiles -- found to be generally similar to those from the Smith *et al.* (1992) study. The hydrometeor profiles themselves were retrieved from the level-2 rain rate profile algorithm of Smith *et al.* (1994a-b, 1998). [This scheme derives cloud microphysical profiles for cloud-radiation databases from the Tripoli (1992a) UW-NMS model run in nested-CRM mode, and can be tailored for use with any type of PMW radiometer and/or radar data.]

In the Smith *et al.* (1992) HH scheme, LH profiles are calculated from vertical derivatives of precipitation mass flux profiles, i.e., separate liquid and frozen hydrometeor mass fluxes with appropriate accounting for the various latent heats of phase change above and below the melting level. Moreover, the algorithm can include the effect of the mass flux of non-precipitating cloud droplets undergoing vertical advection -- assuming a cloud-scale vertical velocity parameter is specified. Noting that all condensation / deposition heating is initiated during formation of non-precipitating hydrometeors, Tao *et al.* (1993b) described an alternate means to account for latent heating due to suspended but vertically advected hydrometeors, i.e., by using coefficients associated with condensation (deposition) of small liquid water droplets (ice particles).

Further development of the HH algorithm, its verification, and global applications are found in the studies of Yang and Smith (1999a-b, 2000). These studies accounted for cloud-scale vertical velocity using a multiple-linear regression equation based on hydrometeor profile densities as the independent variables of regression. For applications with retrievals from TRMM level-2 algorithms, the current scheme uses truncated Legendre polynomial representations of precipitation mass fluxes from surface to precipitation top height (PTH) before

taking vertical derivatives, thus preventing retrieval noise from producing unrealistically large positive / negative heating rates. For applications with the PR or Combined algorithms, no accounting is made for latent heating by deposition-sublimation and freezing-melting processes above and below the melting level since the sensitivity of the TRMM PR is only 17 dBZ -- insufficient for detection of every class of frozen precipitation, particularly smaller and/or less dense graupel particles. For applications with the TMI algorithm, terminal (fall) velocities of precipitating hydrometeors (both rain and graupel) are calculated assuming that the mass spectra of both types of hydrometeor are distributed according to a Marshall-Palmer size distribution function.

2.4 PRH algorithm

The PRH algorithm, as described by Satoh and Noda (2001), uses PR-based retrievals (precipitation profile and convective/stratiform rain fractions) to estimate the vertical LH structure. First, an initial-guess vertical velocity profile is estimated based upon the vertical precipitation structure and convective/stratiform classification. The vertical velocities are used to evaluate a hydrometeor conservation equation under steady state conditions. In stratiform regions, the LH profile is derived directly from the hydrometeor conservation equation (similar to HH algorithm implementation). In convective regions, if a net increase of hydrometeors due to microphysics is inferred from the conservation equation, then the associated LH profile is calculated based upon the vertical motion profile, assuming saturated adiabatic ascent. An iterative method is used to adjust the original vertical motion profile to ensure that vertically integrated net heating and surface rain rates are consistent.

2.5 SLH algorithm

Spectral representation of precipitation profiles obtained from the PR algorithm by use of a small set of distinct profile properties, as reported by Takayabu (2002), provide the basis for the spectral latent heating algorithm (SLH) -- introduced by Shige et al. (2004). This algorithm is currently intended for only PR-retrieved rain rate profiles. Akin to the CSH algorithm, a set of three look-up tables is produced using the GCE model associated with three types of rainfall: (1) convective, (2) shallow-stratiform, and (3) deep anvil stratus. Specifically, however, the look-up tables are indexed according to the vertical information of rain profiles: PTH for convective and shallow stratiform rain, and melting-level rain intensity for anvil (or deep stratiform) rain.

The naming 'spectral' comes from this spectrally indexed table, and it is designed so in order to reduce the dependency of tables on the GCE-CRM simulations of specific field campaigns.

For the first two categories, convective and shallow stratiform, the look-up tables are indexed according to the PTH. For the third category, anvil stratiform rain, the indexing parameter for the associated look-up table is rain rate at the melting level. It is because that PR can measure the perspiration at the melting level as can a ground-based radar (e.g., Leary and Houze 1979), although it cannot observe the PTH accurately enough at the upper-levels of the anvils where small ice-phase hydorometors dominate. Needed inputs for the algorithm are convective/shallow-stratiform/anvil stratus rain index, surface rain rate (Ps), and either PTH or rain rate at the melting level (Pm). The advantage of this scheme is that fundamental heating differences between shallow and deep stratiform rain stages emerge in the diagnosed LH profiles -- stemming from using distinct information concerning the precipitation descriptor (PTH or Pm). Another advantage is that LH profiles arising during the anvil decay stage with no surface rain can be diagnosed, because the normalizing parameter for the tabulated LH profiles (i.e., a denominator) is Pm - Ps -- which does not go to zero if Ps goes to zero.

2.6 Algorithm synthesis

The CSH, GPROF Heating, and SLH algorithms could be used to estimate Q_1 and Q_R along with LH as described in eqn (1), because they use the complete complement of cloud model data generated by CRMs, which includes explicit calculations of the total apparent heat source (Q_1) and its components involving heating due to phase changes of water species (LH), vertical eddy heat flux convergence $\overline{\pi}\left[\overline{\partial w'\theta'/\partial z}\right]$, and radiative heat exchange (Q_R). The estimation of Q_R using these methods introduces new challenges, however, since infrared data (in addition to radar or PMW radiometer data) would be required to infer radiative fluxes from non-precipitating clouds or clear regions. The HH and PRH algorithms estimate only the LH term because they are not explicitly connected to CRM-generated databases, but instead on vertical precipitation mass fluxes either diagnosed from retrieved hydrometeor density profiles (such as those from the TMI algorithm) or calculated directly from retrieved precipitation rates (such as those from the PR or Combined algorithms). Unlike the table look-up approaches, the HH and PRH algorithms calculate LH characteristics directly from vertical gradient structures within precipitation mass flux profiles -- regardless of their source.

A preliminary comparison between earlier versions of three of the algorithms (CSH, GPROF Heating, and HH) was performed for February-1998 TRMM data by Tao *et al.* (2001). The results of the study indicated that the horizontal distributions of latent heat release retrieved by the three schemes were similar and closely related to surface rainfall. They all were able to identify areas of major convective activity, including well-defined sectors of the Intertropical Convergence Zone (ITCZ) within the central and east Pacific, and along the Southern Pacific Convergence Zone (SPCZ). The major differences between the algorithms pertained to the altitude (level) of maximum heating. The CSH estimates exhibited one level of maximum heating with the level varying between different geographic locations -- features in general agreement with diagnostic budget studies. A broader heating maximum, often with two embedded peaks, was generally obtained with the GPROF and HH algorithms, and the sensitivity of the estimated heating profiles to variations in convective activity were less pronounced.

Since all five of the algorithms are still undergoing development and improvement, and since comprehensive intercomparisons of the current versions of the algorithms with independent diagnostic estimates are still to be performed, it is only possible to assign general strengths and weaknesses -- and then in mostly relative terms. In this vein, the effects of the different sets of simplifying assumptions on the various algorithms' LH properties needs careful study. For example, the HH and PRH algorithms are similarly constrained by hydrometeor conservation under a steady-state assumption but under different formulations for LH generation. The other three algorithms are all directly CRM-based, but differ insofar as the cloud type classification schemes, the look-up table indexing strategies, and the detailed properties of the pre-calculated look-up table heating profile entries.

Therefore, the relative accuracy of the methods depends on how representative the tabulated CRM-based profile information and/or dynamical-microphysical simplifying assumptions are for a given situation. Modeling studies based upon CRMs suggest that the instantaneous relationships between hydrometeor profiles and heating profiles at a scale of ~10 km are somewhat ambiguous, and so extraction of specific heating information from a full resolution retrieved hydrometeor profile is problematic. Thus, the use of tabulated heating profiles representing averaged vertical structures for a set of sensor observations, is justified. It is also justified to take space-time averages of instantaneous/footprint-scale estimates over a

specified domain to obtain meaningful estimates, since averaging reduces random error effects. For example, Shige *et al.* (2004) found that spatial averaging of instantaneous/footprint-scale SLH heating estimates over an area of ~50 x 50 km was required to reduce random errors in SLH- reconstructed profiles to acceptable levels.

On the other hand, all algorithms that utilize look-up tables are subject to systematic errors arising from both model deficiencies, and the improper assignment of the tabulated structures to a given set of sensor observations, cloud system type, and climate regime. In some cases, the sensor observations may not provide sufficient information for the algorithm to return unambiguous estimates of heating. For example, artifacts in GPROF Heating estimates arise from the relatively low spatial resolution and thus restricted information content of the TMI's PMW observations (Olson *et al.* 2004). Since TMI observations contain less information regarding both vertical and horizontal hydrometeor structures than PR observations, the GPROF Heating algorithm must rely to a greater extent on its CRM database to physically constrain heating profile estimates, resulting at times in systematic errors. [Note, the main practical advantage of the GPROF algorithm and the CSH and HH algorithms when applied to TMI observations, is that the TMI instrument produces three times the duty cycle of the PR instrument.]

Perhaps the most important source of systematic error arising from current look-up table-based algorithms is that the set of tabulated heating structures do not completely represent the full spectrum of real-atmosphere structures. Since the tabulated structures for the CSH, GPROF Heating, and SLH algorithms are derived from CRM simulations, and since the associated CRM simulations have been performed for only a limited range of environmental conditions and storm-precipitation cases, it is fair to say that no look-up table has yet been created which is fully populated and robust. However, this limitation is expected to be mitigated as greater emphasis is brought to bear on the problem and improved computer technology is used. Ultimately, this will lead to a greater number of CRM simulations, at higher spatial resolutions and increased domain sizes, and with greater consideration given to synthesizing the resultant information content.

3. Diabatic Heating Structures Estimated from Individual Algorithms

Application of the TRMM latent heating algorithms is being conducted over a range of space and time scales, from order 10 to 500 km spatially, and from instantaneous to monthly temporally. Whereas there is no preferred scale for calculating latent heating, but a variety of

applications for the use of latent heating products, research is ongoing to determine the optimal minimal scales at which the latent heating retrievals can be considered reliable.

3.1 Instantaneous latent heating structure

Several of the TRMM latent heating algorithms have been designed to determine instantaneous rain rates and heating profiles at satellite footprint resolution, even though the eventual space-time resolutions may be intended to be evaluated at larger scales -- typically from 0.25 to 5 degrees spatially and from a few hours to monthly temporally. The rationale for operating the algorithms at the highest possible resolutions is that the systematic error in the average of high-resolution estimates of heating is generally less than the systematic error of a single heating estimate made at the scale of the average. Therefore, even though instantaneous, footprint-scale estimates may contain undesirable errors and/or noise, spatial averaging and/or filtering can reduce the random effects to acceptable levels, while ensuring that the smoothed products contain a minimum of systematic error. [Note that frequent temporal sampling is needed whenever a problem involves diurnal variability, which for rainfall processes can be high amplitude over both oceans and continents; see Yang and Smith (2004).]

The major objections to estimating instantaneous latent heating rates at high spatial resolution (say the ~4 km PR nadir beam resolution) is that such estimates either require an assumption of steady-state microphysical conditions (as in HH or SLH), or they will contain significant random errors that must be suppressed by averaging (as in GPROF). The debate on this issue also involves the fact that although microphysical phase changes take place virtually instantaneously and thus embrace the notion that latent heating is an immediate process, the source of latent heating occurs at the microphysical cloud drop/ice crystal nucleation scale. It may be argued that the precipitation distributions that are observed by a spaceborne radars or radiometers are the end product of vertical air motions [strongly linked to latent heating; see Mapes and Houze (1995)] occurring just prior to the observations. Therefore, since the actual latent heating process is not directly detectable by radars or radiometers, it is a certainty that a given algorithm will produce errors in instantaneous estimates since the detection methodology is at least one step removed from the physics of the problem -- regardless of how such errors are mitigated by spatial averaging and/or filtering.

Figure 3 illustrates instantaneous and high resolution (~4 km) rain rates and LH structures is an intense Atlantic tropical cyclone (Hurricane Bonnie) retrieved by the HH algorithm, based

on the vertical derivative of rain mass flux from the Combined TMI-PR rain retrieval algorithm. To suppress spurious noise before taking vertical derivatives, the rain rate profiles used for the calculations are vertically filtered by truncating higher order terms from Legendre polynomial representations of the rain profiles. The structure of the hurricane eye and the convective rain spiral bands are well captured. Rain water appears at high altitudes in the presence of deep convection, such as around 200 km along the track seen in the middle panel of Fig. 3. Widespread weaker rain rates are located between the convective cells. In the weak rain areas, rain rates are mostly concentrated in the middle to lower troposphere where stratiform conditions are prevalent. Deep latent heating is always associated with the strongest convective cells (lower panel of Fig. 3). Peaks of maximum latent heating vary with different conditions. For example, one peak is located at 3-5 km at 180 km along the track, while another is at 3-4 km at 200 km along the track. The altitudes of the LH maxima are generally at or below 5 km. Evaporative cooling occurs in the lower troposphere in these stratiform regions.

Overall, the general structure of latent heating based on the HH algorithm is heuristically correct for a hurricane, although it is important to recognize that the level of maximum heating is lower than found from other studies of tropical cyclones. As noted in section 2.3, this is because the current version of the Combined PR/TMI algorithm (as well as the PR algorithm) does not produce precipitation by any but the largest frozen hydrometeors. By including the effect of all precipitating snow and graupel (that is the non-sensed mass), the level of maximum heating would be elevated. However, because the HH algorithm cannot account for what is not bestowed by the PR insofar as hydrometeor profile completeness, its application with the current versions of the Combined and PR algorithms cannot produce realism in upper-level heating rates. [Note that the next version of the Combined algorithm will include a CRM-based frozen precipitation mode to enable a synthetic (model) account of deposition-sublimation and freezing-melting processes above and below the melting level, ensuring that the HH algorithm will eventually produce complete LH profiles with PR-based precipitation information.]

Presented in Figure 4 are estimates of instantaneous surface rain rate, convective rain rate, and vertical cross-sections (spatially averaged to 28 km) of total rainwater content and $Q1$-QR from an application of the GPROF Heating algorithm. These quantities are derived from TMI observations of a squall line in the tropical North Atlantic Ocean. Heaviest rains are seen along the convective leading edge of the system, while generally lower rain intensities are observed in

the trailing stratiform areas to the north and west of the leading edge. The transect A-B (Fig. 4-panel c) is nearly perpendicular to the leading edge, traversing both the convective and stratiform regions. The leading edge convection is characterized by relatively high rain water contents, exceeding 1 g m^{-3} near the surface. Horizontally collocated with the maximum rain water contents are the maximum estimated heating rates, exceeding 9°C h^{-1} between 5 and 8 km altitude. Stratiform rains (horizontal coordinates less than 120 km) are associated with maximum water contents at midlevels; the decrease of water contents in the lower troposphere is due to evaporation of rain, and cooling rates ~ -1°C h^{-1} are estimated in this region. The overall heating structures are similar to those in Fig. 1, except that the fine features simulated by the GCE-CRM are not observed due to the coarser resolution of the GPROF Heating algorithm's TMI radiance input.

Figure 5a shows instantaneous LH profiles retrieved by both the PRH and SLH algorithms, spatially averaged to 50 km resolution, associated with: (1) a Pacific tropical cyclone (Typhoon Jelawat) in its developing stage (upper diagram), and (2) a mesoscale convective system over the tropical ocean northwest of Australia (lower diagram). The PR-estimated rain rates that are used as input for these two LH algorithms are also shown. Overall, for the tropical cyclone case, there are many similarities between the PRH and SLH profiles. For example, both indicate strong heating on both sides of the eye. In addition, for both algorithms, strong heating is found in a very narrow shaft in the lower troposphere to the right of the eye. Away from the eye/eyewall region, the heating patterns are similar to those observed and simulated by CRMs in the stratiform region of mesoscale convective systems (Houze 1982, 1997; Tao *et al.* 1993b, 2000; Lang *et al.* 2003). On the other hand, there are major differences between the two sets of heating profiles. First of all, PRH heating is confined to the same altitude range with the rainfall profiles, while SLH algorithm retrieve the rainfall well over the rain. This difference is reflected to the larger amplitude at the higher altitudes in horizontal mean profiles in Figure 5a. Secondly, the SLH level of maximum heating is lower than for PRH (examine the upper and lower right-hand panels of the upper diagram). The cooling region retrieved by the PRH algorithm in the lower troposphere is stronger than that of the SLH algorithm. PRH also produces low-level cooling in its convective region -- which is likely spurious. The SLH heating structure has smoother features than PRH because SLH uses a table look-up scheme based on averaged CRM-generated profiles. The general structures of the SLH-generated $Q1$-QR and LH profiles are similar except

that the $Q1$-QR profile exhibits a heating maximum of greater intensity and at a higher altitude (upper-right-hand panel of upper diagram).

The SLH and PRH latent heating analyses associated with an offshore Australian mesoscale convective system are illustrated in the lower diagram of Fig. 5a. Again, the PR-estimated rain rates that are used as algorithm input are shown in the diagram. Strong heating (>10°C h^{-1}) is always associated with large rain rates (> 50 mm h^{-1}) in the convective region of the squall system. There is weak heating aloft and cooling below in the trailing stratiform region. Both averaged $Q1$-QR and LH profiles peak at middle levels (about 6 km according to the upper-right-hand panel of the lower diagram). For this case, the SLH-retrieved level of maximum heating is higher than that of the tropical cyclone case. This is because the convective system is in its mature stage while the tropical cyclone system is in its developing stage. As is evident in the upper-right-hand panel, both the averaged $Q1$-QR and LH profiles peak at middle levels (~6 km). This is in good agreement with the heating maximum found in the mid-troposphere for the Australian Monsoon Experiment (AMEX) convective systems reported by Frank and McBride (1989). The estimated LH profile has a distinct cooling extreme near 4 km due to melting processes. On the other hand, the estimated $Q1$-QR profile does not indicate any cooling near 4 km because the eddy heat flux convergence compensates for the cooling due to melting. As with the tropical cyclone case, PRH yields stronger cooling in the lower troposphere while SLH heating exhibits smoother features.

Figure 5b goes on to show the instantaneous/50 km resolution LH structure of a mid-latitude squall line retrieved using only the PRH algorithm. The PR-observed radar reflectivities and estimated rain rates used as algorithm inputs are also shown. The radar reflectivity pattern is similar to that of an observed PRE-STORM squall line (Rutledge *et al.* 1988). Strong heating (>10°C h^{-1}) is always associated with large rain rates (> 50 mm h^{-1}) at the leading edge of the squall system. There is weak heating aloft and cooling below in the trailing stratiform region. These features are similar to those simulated by CRMs (e.g., Fig. 1b from Lang *et al.* 2003), to observations (e.g., Johnson and Hamilton 1988), and to GPROF retrievals (Fig. 4 cross-section). The LH profile shown in the right-hand panel is also similar to both CRM and observational results.

As Figures 3, 4, and 5a-b illustrate, regardless of the differences in spatial resolution, the instantaneous LH profiles retrieved by the four different heating algorithms qualitatively agree

with one another for insofar as tropical cyclones (HH, PRH, and SLH), oceanic squall lines (GPROF Heating and PRH), and a tropical oceanic MCS (PRH and SLH). Quantitatively, however, there are differences. Some are caused by the different resolutions and filtering techniques employed by the different algorithms, and some by the different algorithm inputs. Foremost are the differing physical assumptions of the algorithms themselves. As a typical example drawn from the above analysis, PRH consistently produces LH profiles with stronger cooling in the lower troposphere. Therefore, a comprehensive algorithm intercomparison using common data sets has been planned for the near future to understand and perhaps mitigate as many of these differences as possible (further discussed in section 5).

3.2 Temporal and spatial averages

The upper three panels of the Cover Figure illustrate 5-year mean apparent heating at three different altitudes (2, 5, and 8 km) over the global tropics from the CSH algorithm using the PR-based level-3 rainfall product. The $Q1$ profiles are calculated by averaging two normalized convective and stratiform kernel heating profiles (scaled according to PR-retrieved surface rain rates and weighted by the convective / stratiform fractions) at a grid scale of 2.5 degrees, for either oceanic or continental conditions. The normalized convective / stratiform kernel profiles are created by averaging all 16 (4) oceanic (continental) base profiles in the CSH algorithm's complete library of 20 heating profile pairs distributed regionally and according to storm type.

As expected from the design of the CSH algorithm, the horizontal distribution of the estimated $Q1$ structure is similar to the pattern of surface rainfall (lower panel of the Cover Fig.), especially at middle and upper levels. For example, a well defined ITCZ in the east and central Pacific Ocean and Atlantic Ocean, a well-defined SPCZ in the central-southern Pacific Ocean, and broad areas of precipitation events spread over the continental regions are all evident. Also, strong latent heat release in the middle and upper troposphere (5°C day^{-1} and greater) is always associated with heavier surface precipitation. Heating in the upper troposphere over the Pacific and Indian Oceans covers a much broader area than the heating over Africa, South America, and the Atlantic Ocean. Notably, the clearly evident differential heating distribution between land and ocean in the upper troposphere is capable of generating strong horizontal gradients in the thermodynamic fields that can then interact with the global circulation.

An interesting feature seen in the Cover Fig. is the relatively weak heating-cooling behavior (-1 to 1°C day^{-1}) at 2-km over the Pacific and Indian Oceans. This may be due to the

moisture content over the Pacific being generally high and concomitant cooling by evaporation of rain drops in the lower troposphere being weak over moister areas. Another explanation is that convective heating and stratiform cooling in the lower troposphere compensate one another.

Figure 6 shows the 5-year vertical average $Q1$ profiles for spring, summer, autumn, and winter over the entire global tropics -- plus the continents and oceans separately. Globally, the summer and autumn seasons show stronger heating associated with heavier rainfall. Over land, the summer season exhibits the strongest heating. Heating patterns during the spring and autumn seasons are similar. Significant cooling in the lower troposphere occurs over the continents but not over the oceans. The level of maximum heating and its magnitude over the oceans separately are very similar to the global average because 70% of the Tropics is covered by ocean.

Figure 7 illustrates the $Q1$ structures associated with two climate events, an El Niño episode from December 1997 through February 1998 and a La Niña episode from December 1998 through February 1999. The diagrams in the two left-hand panels show retrieved heating anomalies for the two events (relative to a 3-year mean commencing Dec'97), with the greatest anomalies occurring over the equatorial Pacific, west Pacific, and Indian Oceans. The $Q1$ patterns over the maritime continent, North America, and Africa are similar. Monthly time series of $Q1$ profiles over the tropics and their deviations from the 3-year mean are shown in the right-hand panel of Fig. 7. The level of maximum heating is approximately 7.5 km. The variations of the level of maximum heating and its magnitude are small. This is because global tropical rainfall accumulations for El Niño and La Nina are virtually identical as observed by the PR. However, there are cold and warm anomalies during the El Niño and La Niña periods. These features are due to the fact that the PR observes a higher percentage of stratiform precipitation during the El Niño episode, which leads to stronger retrieved low-level cooling as compared to La Niña.

4. Validation of Algorithms

Validation of LH profiles retrieved from satellite is not straightforward because there is no instrument (i.e., no "*latent-heatometer*") or direct means to measure this quantity, and as a result, there is no primary calibration standard by which the validation process can be adjudicated. This is mainly because diagnostic heat budget analysis is not an exact science (Mapes et al. 2003). Thus, just as satellite rainfall retrieval must rely on indirect strategies to achieve validation (Smith and Hollis 2003), latent heating retrieval must also rely on indirect approaches.

4.1 Comparing CRM heating with algorithm-reconstructed & diagnostically-estimated heating

Consistency checking involving CRM-generated heating profiles and both algorithm-reconstructed and diagnostically-estimated heating profiles is a useful step in evaluating the performance of a given latent heating algorithm. In this process, the CRM simulation of a time-dependent precipitation process (multiple-day time series) is used to obtain the required input parameters for a given latent heating algorithm. The algorithm is then used to "reconstruct" the heating profiles that the CRM simulation originally produced, and finally both these sets of conformal estimates (model and algorithm) are compared against coincident estimates of diagnostically-based heating derived from rawinsonde observations. Such observations from various field experiments, as well as simulations of individual precipitation systems, have been used for such consistency checks (Tao *et al.* 1993b, 2000; Olson *et al.* 1999, 2004; Shige *et al.* 2004).

In the following two examples, diagnostic results from the TOGA-COARE Intensive Flux Array (IFA) for 19-27 December 1992 (refer to Fig. 2) are used for consistency checking with both the CSH and SLH algorithms. In the first example, Figure 8 illustrates the evolution of Q_1 heating reconstructed by the CSH algorithm from GCE-CRM simulation data, averaged over the TOGA-COARE IFA. The algorithm-reconstructed profiles are in close agreement to those determined diagnostically from soundings, as well as to those from the original GCE-CRM simulation. This is evident by comparing the Fig. 8 with the Fig. 2 results and noting that the 30-minute filtering first applied to the GCE-CRM time series is also applied to the reconstructed time series. [Heating profiles selected in the CSH algorithm's look-up table are GCE-CRM time-averaged (6-hour) heating profiles from 19-27 December 1992.] As noted, the heating profiles based on the GCE-CRM should be in close agreement with those from the diagnostic calculations, because the GCE model is driven by large-scale advective forcing in temperature and water vapor, and therefore the model's simulated rainfall is just the response to that forcing. However, using simulation output from the GCE-CRM as a means to parameterize the CSH heating algorithm does not necessarily guarantee accurate Q_1 retrievals. For example, errors in surface rain rates as determined from the accompanying rain algorithm can lead to errors in retrieving heating magnitudes along the vertical profile, while errors in convective/stratiform rainfall fractions via classification can lead to errors in retrieving the levels of maximum heating.

In the second example, Figure 9 shows analogous information for both the CSH and SLH algorithms, except in terms of latent heating, and in direct comparison to the equivalent quantity from a GCE-CRM simulation. Whereas Q_1 and Q_R can be similar order terms over regional domains for extended space and time periods (e.g., Smith 1986, and Smith and Shi 1995), for mesoscale convection and precipitation processes, the difference between column-integrated Q_1 and LH is small. This is because LH, which generally ranges from 10-50°C day^{-1}, dominates over Q_R (which is typically a cooling process of some 0.5-2.0°C day^{-1}) and over $\overline{\pi}\,\overline{[\partial w'\theta'/\partial z]}$ (which can be negligible during certain types of active convective events such as those found by Soong and Tao 1980 and Johnson *et al.* 2002). [These scale relationships are illustrated in Figure 10 based on the GATE cloud modeling analysis of Tao and Soong (1986).]

It is evident in Fig. 9 that the temporal variations of both the CSH- and SLH-reconstructed profiles are generally similar to variations in the GCE-CRM-simulated profiles. In particular, both the CSH- and SLH-reconstructed profiles capture the evolution of a quasi-2-day oscillation which occurred during the period 1800 UTC 23 - 1800 UTC 25 December 1992, an oscillation that had been noted earlier by Takayabu *et al.* (1996). As pointed out by Shige et al. (2004), there are noteworthy improvements in the SLH-reconstructed profiles for the shallow-convective stage from 1800 UTC 23 to 0600 UTC 24 December 1992 and the anvil decay stage from 0600 UTC to 1800 UTC 25 December 1992. Shallow convection can be retrieved by the SLH algorithm, because it uses observed information on precipitation depth (i.e. PTH). Heating profiles in the decaying stage with no surface rain (e.g., 1200 UTC 25 December) can also be retrieved by the SLH algorithm. This comes from utilizing the precipitation rate at the melting level for anvil rain. Also, both the CSH- and SLH-reconstructed results are smoother than the GCE-CRM calculations because the associated lookup tables contain averaged profiles for each height index.

4.2 Explicit comparison of satellite retrievals with diagnostic calculations

Several TRMM field campaigns, specifically SCSMEX, TRMM-LBA, and KWAJEX, were conducted between May 1998 and September 1999, focusing on validation of TRMM rainfall products (i.e., vertical hydrometeor and rain rate profiles, and vertical distribution of latent heating). Since LH profiles cannot be directly measured, CRMs are needed in designing LH algorithms to provide the link between rain rate structures and LH structures. Consequently, one of the key objectives behind the TRMM field campaigns was to obtain observations of the thermodynamical, dynamical, and microphysical structure and evolution of MCSs, as well as

individual convective clouds and the large-scale environments in which they were embedded. CRMs require such observations for initial conditions, as well as for validation of model-diagnosed latent heating.

Figure 11 draws attention to why a variety of field campaigns are so important in the development and validation of LH algorithms. The four pairs of diagrams in the figure illustrate fundamental differences in the characteristic organization of precipitating convective systems as observed and simulated in the three aforementioned TRMM field campaigns, as well as in a DOE-ARM field campaign conducted in June 1997. The instantaneous model realizations of precipitation conditions for the four different cases emphasize the underlying variants within the general organizational structure of convective storms.

Regarding the two western Pacific cases in Fig. 11, the SCSMEX simulation exhibits an intense tropical squall line structure without significant stratiform cover, whereas the KWAJEX simulation exhibits a more random distribution of convective cells with extensive stratiform debris. For both of these tropical ocean cases, which describe the respective dominant modes of rainfall behavior associated with the two study regions, most of the surface precipitation originates as graupel. For the North American mid-west continental DOE-ARM case, the storm also develops as a squall line. However, it is considerably weaker than the SCSMEX case, but at the same time exhibits more instability and precipitation downstream of the propagating convective line. For the two TRMM-LBA cases, consisting of both easterly and westerly regime MCSs, the westward propagating storm is long-lived, well-organized, juxtaposed with a massive gravity outflow boundary, and exhibits microphysical properties of a maritime MCS. Conversely, the westerly regime case appears as a shorter-lived, fractured, smaller, more linear precipitation structure, displaying weaker convection without any well-defined outflow boundary, and exhibits the microphysical properties of a continental storm with high cloud bases (i.e., a deeper boundary layer). [The studies of Halverson et al. (2002) and Petersen et al. (2002) have investigated, in detail, the contrasting meteorological properties of central Amazon's easterly and westerly storm regimes.]

In considering the detailed LH properties associated with various observation periods of the TRMM field campaigns, Figures 12a-b illustrate the variability of rainfall (Fig. 12a) and apparent heating (Fig. 12b) within the KWAJEX study area during the course of three separate time sequences from the campaign's intensive observational period (IOP). In Fig. 12a, rainfall

observations are obtained from both the Kwajalein dual-polarization Doppler radar (KPOL), and the standard TRMM PR-only algorithm. In Fig. 12b, the 5-day, 3-day, and 15-day sequences are periods during which the meteorological sounding data were of sufficient quality to make calculations of the $Q1$ budget, while at the same time specifying initial conditions for integrations of the GCE-CRM, i.e., calculations to be compared to the sounding budgets.

The salient features seen in the various diagrams of Figs. 12a-b are: (1) the KPOL and PR radars' rain rate estimates are fairly consistent, considering their different viewing perspectives and measuring frequencies, (2) the differences between the 2D and 3D GCE-CRM simulated rain rates are largely negligible, denoting that latent heating rates reported in earlier 2-dimensional CRM literature, before 3-dimensional modeling became computationally practical, are likely representative, (3) the GCE-CRM hourly rain rates are in close correspondence with the KPOL radar's hourly rain rates, denoting that the modeled, vertically-integrated apparent heating rates are also likely to be sound, (4) the diagnostically-derived and GCE-CRM $Q1$ calculations are in excellent quantitative agreement, as perhaps could be anticipated given the prior result, particularly for the three ITCZ excitation periods (monsoon flow regimes) occurring on August 11, August 19, and September 2 -- but also for moderate and weak convective systems, (5) the agreement between diagnosed and modeled apparent heating rates vary from poor to good during periods of negative $Q1$ heating, i.e., when radiative cooling processes dominate for suppressed convection conditions (subsiding troposphere) or for cloud-top radiative cooling in the presence of weak convection when upper cloud latent heating rates are small, reinforcing the view of many that accurately simulating radiative transfer in partly cloudy tropical atmospheres remains elusive, and finally (6) at the scale of the KPOL radar observing domain, latent heating is a stochastic process, with individual layer LH rates modulating from approximately -7 to 70°C day^{-1}. These KWAJEX results draw attention to how important accurate rain retrieval is to satellite-based latent heating estimation, plus they provide motivation for employing high spatial resolution in the retrieval process to account for the intrinsic spatial heterogeneity of the heating field.

Switching the focus to the SCSMEX field campaign and actual explicit validation of TRMM algorithm heating retrievals based on diagnostic calculations, Figure 13 shows a comparison between CSH and GPROF Heating algorithm-retrieved heating, sounding-based (diagnostic) heating, and GCE-CRM-based heating during SCSMEX's most convectively active

period (May 15 - June 20 1998). The study area for this comparison takes place over SCSMEX's Northern Enhanced Sounding Area (NESA), a ~6 x 10 deg latitude-longitude box in the northern oceanic region of the South China Sea. As emphasized in the discussion of Fig. 11, because of the significant variability of convective systems, selecting appropriate heating profiles from the CSH algorithm's look-up table for specific convective events is non-trivial. For this comparison, two different approaches for selecting tabulated profiles have been used. In the first approach, normalized heating profiles representing general tropical oceanic (gto) conditions are obtained by averaging profiles from a look-up table based on a set of diagnostic studies and a growing (but still limited) set of GCE-CRM simulations -- see Figs. 3 and 4 in Tao *et al.* (2000). In the second approach, normalized heating profiles representing South China Sea (scs) conditions and indexed according to geographic location and month-of-year, are used. Regarding GPROF, a climatological radiative heating profile is added to the GPROF estimates of Q_1-Q_R to obtain an approximate Q_1, which can be more directly compared to the rawinsonde diagnostic estimates; Olson *et al.* (2004). The CRM database used in the GPROF algorithm is the standard 2a12 operational database.

For the CSH-gto approach, the algorithm-retrieved $Q1$ heating magnitudes are somewhat greater than the sounding-derived magnitudes. Nevertheless, there is agreement insofar as various key features of the vertical profiles, particularly concerning the level of maximum heating and the slight boundary layer cooling feature. For the CSH-scs approach, the retrieved profile magnitudes are in better agreement with the sounding-derived estimates, particularly in the upper troposphere where the retrieved and diagnostic magnitudes are in close correspondence -- but also in both the middle and much of the lower troposphere. On the other hand, the second approach exhibits greater departures insofar as boundary layer cooling, and also indicates a level of maximum heating some 0.5-1 km lower than the diagnostic calculation. This latter difference is consistent with the GCE-CRM-simulated level of maximum heating -- also being some 0.5-1 km lower than the diagnostic calculation. Of interest is that the difference between the GCE-CRM profile and the diagnostic profile is effectively opposite to that of the difference between the CSH-scs profile and the diagnostic profile, i.e., the GCE-CRM result is in closest correspondence in the middle and lower troposphere with larger differences in the upper troposphere. Neither of the two CSH approaches replicate the relative heating maximum at

~15.5 km seen in the diagnostic profile. [See Tao *et al.* (2003b) for further discussion concerning this SCSMEX intercomparison.]

The mean GPROF Heating profile for the same SCSMEX period is similar in structure to the diagnostic profile (i.e., broad agreement between the level of maximum heating and boundary layer cooling). The salient differences are that in the boundary layer and just below the freezing level, GPROF cooling is greater than found in either the CSH-gto or diagnostic results. Although not yet fully understood, these cooling features are attributed to biases in the algorithm's CRM database, coupled with the limited information content of the radiometer data. The aim of a future investigation by the authors will be to identify and correct biases in the current physical parameterizations of CRM's, as they pertain to the simulation of microphysical and latent heating distributions. A more in-depth analysis of the GPROF heating comparisons to SCSMEX NESA data can be found in Olson *et al.* (2004).

5. Global Modeling Applications

Whereas assimilation of TRMM rainfall data has proven to be an effective technique for improving predictive skill in global weather prediction models (e.g., see Bauer *et al.* 2002; Hou *et al.* 2000a-b, 2001, 2004; Krishnamurti *et al.* 2000a-b, 2001; and Marecal *et al.* 2002), use of explicit latent heating information for initialization and/or assimilation in global models is a research topic just beginning to re-emerge. The recent studies are motivated by early pioneering research in latent heating assimilation by Wang and Warner (1988), Puri and Miller (1990), Raymond et al. (1995), and others. Two global models, one from Florida State University (FSU) and the other from the NASA/Goddard Space Flight Center (GSFC), are currently using TRMM-based LH data sets to improve cumulus parameterization schemes and identify physical shortcoming with such schemes.

At this stage it appears that the direct use of satellite (and or other ground-based) diabatic heating profile information for atmospheric modeling requires a physical initialization design. For example, T.N. Krishnamurti and his colleagues at FSU, using the Krishnamurti *et al.* (1991) global-spectral model as the host, have developed a new experimental cumulus parameterization scheme -- aptly called ECPS. This scheme uses past model analysis data sets to relate $Q1$-QR heating to TRMM-retrieved latent heating. In closing this problem, they have found it necessary to use a limited number of vertical modes (expressed by a few empirical orthogonal functions) to relate model-generated heating to its satellite-observed counterpart. During a training phase, $Q1$

and $Q2$ profiles drawn from TRMM data sets coincident with profiles from ECMWF analyses were acquired. After rotated principal component (RPC) analyses were performed on the heating ($Q1$) and drying ($Q2$) profiles over tropical convective regions, the first three RPC modes were found to explain most of the meaningful observational variance. Expressing $Q1$ and $Q2$ profiles as a linear combination of the first three dominant RPCs produced close agreement in associating the large-scale variables. Tests now being conducted with the ECPS parameterization scheme in conjunction with the $Q1$ - $Q2$ estimation scheme are producing realistic vertical distributions of heating and drying for a cumulus environment.

As shown in Figure 14, preliminary tests with ECPS result in improved precipitation and circulation predictions at 48 and 72 hours. This suggests that explicit assimilation of satellite-retrieved LH profiles is a promising new avenue of NWP research. Obviously, further studies are needed to quantify how much prediction improvement can be obtained in moving from surface rainfall-based data assimilation (and/or PMW radiance-based assimilation) to LH-based data assimilation. However, in purely theoretical terms, it is the vertical distribution of diabatic heating that lies at the heart of the key underlying physical process that has never been resolvable using standard observations (from either soundings or weather satellite data) for model initialization and/or assimilation.

Research is also taking place at GSFC to develop variational techniques to assimilate TMI-derived convective and stratiform LH rates within the general framework of parameter estimation, using disposable parameters in the relevant moist physics scheme as the control variables. The focus is to explore the feasibility of improving global climate analyses and weather forecasts through the assimilation of satellite-retrieved LH profiles that are radiatively compatible with multichannel PMW radiometer radiances. Such optimization of physical parameterizations in the context of data assimilation can provide valuable information for diagnosing model deficiencies and guiding the improvement of the parameterization schemes.

There is a final application worth mentioning, also involving NWP modeling, in which satellite-retrieved LH profiles represent an important commodity. As the number of NWP models subjected to initialization by retrieved LH profiles increases, substantive improvements in forecasting capabilities via "superensemble" techniques are expected to take place. The superensemble approach has been invoked as a powerful tool for improving the robustness of weather and climate forecasts, as has been emphasized in studies from the FSU modeling group

(viz., Krishnamurti *et al.* 2000a-b; Vijaya Kumar *et al.* 2003; Williford *et al.* 2003; Yun *et al.* 2003). The goal of superensemble forecasting is to reduce overall uncertainties -- as well as to better estimate errors associated with the various models, their physical parameterizations, and the ingested data sets. Thus, to the degree that satellite LH profiles can constrain initialization of forecasts and/or guide initializations through pre-forecast assimilation periods, superensemble forecasting may be able to exploit satellite-retrieved LH products in further reducing uncertainties for ensemble problems that are particularly sensitive to diabatic heating processes.

6. Recommended Future Research

Three of the TRMM LH algorithms (i.e., CSH, GPROF Heating, SLH) require CRM-simulated cloud data sets involving pre-calculated heating profiles. As noted earlier, given the concern with systematic errors arising from too few available CRM simulations creating scarcity effects in the data bases, the number of heating profiles associated with different types of clouds and convective systems occurring at a variety of geographic locations and throughout the seasonal cycle, will eventually have to be increased. Observations from additional field experiments will also have to be used to provide new types of initial conditions for the CRMs, as well as to help validate the CRM-simulated LH calculations themselves. Heating profiles obtained from numerical model simulations and large-scale model reanalyses should also be compared with those from the CRMs and the associated retrieval algorithms.

Such comparisons will help identify the salient physical processes leading to similarities and differences produced by the CRMs and the retrieval algorithms. In addition, data from field campaigns that provide extensive and high quality *in situ* microphysical observations, including TRMM-LBA and KWAJEX, will be useful in validating and improving CRM-generated microphysics. Marzano et al. (1996), Panegrossi *et al.* (1998), Smith et al. (2002), and Fiorino and Smith (2004) have already addressed various issues concerning how improved microphysical representations in radiative transfer models can improve microwave-based precipitation retrieval. This is important because representative microphysics is essential in reproducing, within a modeling framework, the key four-dimensional features of latent heating.

It is also important that diagnostically-based heating profiles obtained during the TRMM field campaigns, as well as from other field campaigns such as those conducted by the DOE-ARM program, be compared to corresponding heating profiles from the different TRMM algorithms to ensure thorough validation. In this type of validation study, Doppler radar observations, particularly dual-Doppler observations that can accurately resolve the horizontal mesoscale wind field, would be extremely valuable (e.g., see DOE-ARM related paper by Clothiaux et al. 2000), although the greater abundance of single-Doppler observations, which can be also be used to infer horizontal wind divergence and vertical motion (related to diabatic heating), should also be exploited (e.g. Mapes and Lin, 2004). Doppler radar comparisons could help quantify errors within the current LH algorithms and help guide the way to the development of a next generation of algorithms.

Notably, as a follow-up to this study, a comprehensive intercomparison between the different LH algorithms for various common TRMM data sets is now planned for 2005. This study will consider the major heat and moisture budget terms, i.e., LH, Q_1, Q_R, and $\overline{\pi}\overline{[\partial w'\theta'/\partial z]}$. Also, global analyses will be used to identify and compare the large-scale circulation patterns for important retrieval periods and for key periods of earlier field campaigns including the GATE and TOGA-COARE tropical ocean field campaigns. These will be useful because in extending what is learned from local field campaign observations to other parts of the tropics where campaigns have yet to be conducted, use of latent heating "similarity" assumptions are inviting. However, whereas it might be reasonable to expect that LH structures associated with distinct tropical oceanic phenomena such as westerly wind bursts or super cloud clusters (that usually arise under comparable large-scale circulation fields with similar SST conditions) might not be all that different (e.g., Lau *et al.* 1989), these assumptions deserve careful attention. Since all the algorithms can all produce instantaneous LH profiles at the scale of the satellite footprint, and given that spatial averaging is effective in reducing noise in instantaneous heating profiles, identification of an optimal spatial scale and selection of appropriate filters for use with instantaneous LH algorithms is another important issue that needs resolution and consensus in the future study.

Once such research is completed and likely during the 2005 time frame, the first standard LH products for TRMM will be publicly released. This represents a welcome step because widespread dissemination of high resolution, globally-distributed, and continuous LH information to the research community, a data product that a decade ago was considered beyond reach, will enable compelling new investigations into the thermo-hydro-dynamical complexities of storm life cycles, diabatic heating controls and feedbacks related to meso-synoptic circulations, and the influence of diabatic heating on the atmospheric general circulation and the Earth's climate system in general.

7. Acknowledgements

The authors extend their appreciation to Professors Robert Houze of the University of Washington, Richard Johnson of Colorado State University, Michio Yanai of the University of California at Los Angeles, and Edward Zipser of the University of Utah whose willingness over the years to discuss their ideas concerning atmospheric latent heating has had profound influence on various ideas central to this paper. This research has been supported by an assortment of TRMM Science Team grants under the auspices of both the National Aeronautics and Space Administration (NASA) and the Japan Aerospace Exploration Agency (JAXA). The authors wish to thank to Drs. Kwo-Sen Kuo and Chung-Lin Shie of the NASA/Goddard Space Flight Center for preparing the Cover Figure and Figure 12, respectively, and to Mr. Ken'ichi Ito of the Remote Technology Center of Japan for preparing Figure 5.

8. References

Adler, R.F., and E.B. Rodgers, 1977: Satellite-observed latent heat release in a tropical cyclone. *Mon. Wea. Rev.*, **105**, 956–963.

Bauer, P., J.-F. Mahfouf, W.S. Olson, F.S. Marzano, S. DiMichele, A. Tassa, and A. Mugnai, 2002: Error analysis of TMI rainfall estimates over ocean for variational data assimilation. *Quart. J. Roy. Meteor. Soc.*, **128**, 2129-2144.

Biggerstaff, M. I., and R. A. Houze, Jr., 1991: Kinematic and precipitation structure of the 10-11 June 1985 squall line. *Mon. Wea. Rev.*, **119**, 3034-3065.

Chong, M., and D. Hauser, 1990: A tropical squall line observed during the COPT 81 experiment in West Africa. Part III: Heat and moisture budgets. *Mon. Wea. Rev.*, **118**, 1696–1706.

Clothiaux, E.E., T.P. Ackerman, G.G. Mace, K.P. Moran, R.T. Marchand, M.A. Miller, and B.E. Martner, 2000: Objective determination of cloud heights and radar reflectivities using a combination of active remote sensors at the ARM CART sites. *J. Appl. Meteor.*, **39**, 645–665.

Cunning, J.B., 1986: The Oklahoma-Kansas Preliminary Regional Experiment for STORM-Central. *Bull. Amer. Meteor. Soc.*, **67**, 1478–1486.

Dudhia, J., 1993: A nonhydrostatic version of the Penn State-NCAR Mesoscale Model: Validation tests and simulation of an Atlantic cyclone and cold front. *Mon. Wea. Rev.*, **121**, 1493-1513.

Emanuel, K.E., J.D. Neelin, and C.S. Bretherton, 1994: On large-scale circulations in convecting atmospheres. *Quart. J. Roy. Meteor. Soc.*, **120**, 111-1143.

Fiorino, S.T., and E.A. Smith, 2004: Critical assessment of microphysical assumptions within TRMM-radiometer rain profile algorithm using satellite, aircraft & surface data sets from KWAJEX. *J. Appl. Meteor.*, accepted.

Frank, W.M., and J.L. McBride, 1989: The vertical distribution of heating in AMEX and GATE cloud clusters. *J. Atmos. Sci.*, **46**, 3464-3478.

Gallus, W.A., and R.H. Johnson, 1991: Heat and moisture budgets of an intense midlatitude squall line. *J. Atmos. Sci.*, 122–146.

GATE-ISMG (J.P. Kuettner, D.E. Parker, D.R. Rodenhuis, H. Hoeber, H. Kraus, and S.G.H. Philander), 1974: GATE. *Bull. Amer. Meteor. Soc.*, **55**, 711–744.

Hack, J.J., and W.H. Schubert, 1990: Some dynamical properties of idealized thermally–forced meridional circulations in the tropics. *Meteorol. Atmos. Phys.*, **44**, 101–118.

Haddad, Z.S., E.A. Smith, C.D. Kummerow, T. Iguchi, M.R. Farrar, S.L. Durden, M. Alves, and W.S. Olson, 1997: The TRMM 'Day-1' radar/radiometer combined rain-profiling algorithm. *J. Meteor. Soc. Japan*, **75**, 799-809.

Halverson, J.B., T. Rickenbach, B. Roy, H. Pierce, and E. Williams, 2002: Environmental characteristics of convective systems during TRMM-LBA. *Mon. Wea. Rev.*, **130**, 1493–1509.

Hartmann, D.L., H.H. Hendon, and R.A. Houze, Jr., 1984: Some implications of mesoscale circulations in tropical cloud clusters for large-scale dynamics and climate. *J. Atmos. Sci.*, **41**, 113-121.

Hou, A.Y., S.-Q. Zhang, A.M. da Silva, and W.S. Olson, 2000a: Improving assimilated global data sets using TMI rainfall and columnar moisture observations. *J. Clim.*, **13**, 4180-4195.

Hou, A.Y., D.V. Ledvina, A.M. da Silva, S.-Q. Zhang, J. Joiner, R.M. Atlas, G.J. Huffman, and C.D. Kummerow, 2000b: Assimilation of SSM/I-derived surface rainfall and total precipitable water for improving the GEOS analysis for climate studies. *Mon. Wea. Rev.*, **128**, 509-537.

Hou, A.Y., S.-Q. Zhang, A.M da Silva, W.S. Olson, C.D. Kummerow, and J. Simpson, 2001: Improving global analysis and short-range forecasts using rainfall and moisture observations derived from TRMM and SSM/I passive microwave sensors. *Bull. Amer. Meteor. Soc.*, **82**, 659-679.

Hou, A.Y., S.-Q. Zhang, and O. Reale, 2004: Variational continuous assimilation of TMI and SSM/I rain rates: Impact on GEOS-3 hurricane analyses and forecasts. *Mon. Wea. Rev.*, submitted and in revision.

Houze, R.A., Jr., and A.K. Betts, 1981: Convection in GATE. *Revs. Geophys.*, **19**, 541-576.

Houze, R.A., Jr., 1982: Cloud clusters and large-scale vertical motions in the tropics. *J. Meteor. Soc. Japan*, **60**, 396-409.

Houze, R.A., Jr., and E.N. Rappaport, 1984: Air motions and precipitation structure of an early summer squall line over the eastern tropical Atlantic. *J. Atmos. Sci.*, **41**, 553–574.

Houze, R.A., Jr., 1989: Observed structure of mesoscale convective systems and implications for large-scale heating. *Quart. J. Roy. Meteor. Soc.*, **115**, 425-461.

Houze, R.A., Jr., 1997: Stratiform precipitation in regions of convection: A meteorological paradox. *Bull. Amer. Meteor. Soc.*, **78**, 2179-2196.

Iguchi, T., T. Kozu, R. Meneghini, J. Awaka, and K. Okamoto, 2000: Rain-profiling algorithm for the TRMM precipitation radar. *J. Appl. Meteor.*, **39**, 2038-2052.

Johnson, D., W.-K. Tao, J. Simpson, and C.-H. Sui, 2002: A study of the response of deep tropical clouds to large scale processes. Part I: Model set-up strategy and comparison with observations. *J. Atmos. Sci.*, **59**, 3492-3518.

Johnson, R.H., 1984: Partitioning tropical heat and moisture budgets into cumulus and mesoscale components: Implication for cumulus parameterization. *Mon. Wea. Rev.*, **112**, 1656-1665.

Johnson, R.H., and P.J. Hamilton, 1988: The relationship of surface pressure features to the precipitation and airflow structure of an intense midlatitude squall line. *Mon. Wea. Rev.*, **116**, 1444-1472.

Johnson, R.H., and P.E. Ciesielski, 2002: Characteristics of the 1998 summer monsoon onset over the Northern South China Sea. *J. Meteor. Soc. Japan*, **80**, 561-578.

Jorgensen, David P., LeMone, Margaret A., Trier, Stanley B. 1997: Structure and Evolution of the 22 February 1993 TOGA COARE Squall Line: Aircraft Observations of Precipitation, Circulation, and Surface Energy Fluxes. *J. Atmos. Sci.,* **54**, 1961-1985.

Kozu, T., and Coauthors, 2001: Development of Precipitation Radar on-board the Tropical Rainfall Measuring Mission (TRMM) satellite. *IEEE Trans. Geosci. Rem. Sens.*, **39**, 102-116.

Krishnamurti, T.N., J.S. Xue, H.S. Bedi, K. Ingles, and D. Oosterhof, 1991: Physical initialization for numerical weather prediction over the tropics. *Tellus*, **43**, 53-81.

Krishnamurti, T.N., C.M. Kishtawal, Z. Zhang, T. LaRow, D. Bachiochi, E. Williford, S. Gadgil, and S. Surendran, 2000a: Multimodel ensemble forecasts for weather and seasonal climate. *J. Clim.*, **13**, 4196–4216.

Krishnamurti, T.N., C.M. Kristawal, D.W. Shin, and C.E. Willford, 2000b: Improving tropical precipitation forecasts from a multianalysis superensemble. *J. Clim.*, **13**, 4217-4227.

Krishnamurti T.N., S. Surendran, D.W. Shin, R.J. Correa-Torres, T.S.V. Vijaya Kumar, E. Williford, C. Kummerow, R.F. Adler, J. Simpson, R. Kakar, W.S. Olson, and F.J. Turk, 2001: Real-time multianalysis-multimodel superensemble forecasts of precipitation using TRMM and SSM/I products. *Mon. Wea. Rev.*, **129**, 2861-2883.

Kummerow, C., W.S. Olson, and L. Giglio, 1996: A simplified scheme for obtaining precipitation and vertical hydrometeor profiles from passive microwave sensors. *IEEE Trans. Geosci. Rem. Sens.*, **34**, 1213-1232.

Kummerow, C., W. Barnes, T. Kozu, J. Shiue, and J. Simpson, 1998: The Tropical Rainfall Measuring Mission (TRMM) sensor package. *J. Atmos. Oceanic Tech.*, **15**, 809-817.

Kummerow, C., Y. Hong, W. S. Olson, S. Yang, R. F. Adler, J. McCollum, R. Ferraro, G. Petty, D.-B. Shin, and T. T. Wilheit, 2001: The evolution of the Goddard Profiling Algorithm (GPROF) for rainfall estimation from passive microwave sensors. *J. Appl. Meteor.*, **40**, 1801-1820.

Lang, S., W.-K. Tao., J. Simpson, and B. Ferrier, 2003: Numerical modeling of convective-stratiform precipitation processes: Sensitivity to partition methods. *J. Appl. Meteor.*, **45**, 505-527.

Lau, K.-M., and L. Peng, 1987: Origin of low-frequency (intraseasonal) oscillations in the tropical atmosphere. Part I: Basic theory. *J. Atmos. Sci.*, **44**, 950-972.

Lau, K.-M., and P.H. Chan, 1988: Intraseasonal and interannual variations of tropical convection: A possible link between the 40-day mode and ENSO. *J. Atmos. Sci.*, **45**, 950-972.

Lau, K.-M., L. Peng, C.H. Sui, and T. Nakazawa, 1989: Dynamics of super cloud clusters, westerly wind bursts, 30-60 day oscillations and ENSO: An unified view. *J. Meteor. Soc. Japan*, **67**, 205-219.

Lau, K.M., Y. Ding, J.-T. Wang, R. Johnson, T. Keenan, R. Cifelli, J. Gerlach, O. Thiele, T. Rickenbach, S.-C. Tsay, and P.-H. Lin, 2000: A report of the field operations and early results of the South China Sea Monsoon Experiment (SCSMEX). *Bull. Amer. Meteor. Soc.*, **81**, 1261–1270.

Leary, C. A., and R. A. Houze, Jr., 1979: Melting and evaporation of hydrometeors in precipitation from the anvil clouds of deep tropical convection. *J. Atmos. Sci.*, **36**, 669-679

Lin, X., and R.H. Johnson, 1996: Heating, moistening and rainfall over the western Pacific during TOGA COARE. *J. Atmos. Sci.*, **53**, 3367-3383.

Lipps, F.B., and R.S. Hemler, 1986: Numerical simulation of deep tropical convection associated with large-scale convergence. *J. Atmos. Sci.*, **43**, 1796-1816.

Mapes, B. E., and R. A. Houze, Jr., 1995: Diabatic divergence profiles in western Pacific mesoscale convective systems. *J. Atmos. Sci.*, **52**, 1807-1828.

Mapes, B. E., and J. Lin, 2004: Wind divergence – rainfall relationships in 9919 hours of tropical single Doppler radar data. *Mon. Wea. Rev.* (submitted).

Mapes, B.E., P.E. Ciesielski, and R.H. Johnson, 2003: Sampling errors in rawinsonde-array budgets. *J. Atmos. Sci.*, **60**, 2697–2714.

Marecal, V. J.-F. Mafouf, and P. Bauer, 2002: Comparison of TMI rainfall estimates and their impact on 4D-Var assimilation. *Quart. J. Roy. Meteor. Soc.*, **128**, 2737-2758.

Marzano, F.S., A. Mugnai, G. Panegrossi, N. Pierdicca, E.A. Smith, and J. Turk, 1999: Bayesian estimation of precipitating cloud parameters from combined measurements of spaceborne microwave radiometer and radar. *IEEE Trans. Geosci. Rem. Sens.*, **37**, 596-613.

Meneghini, R., T. Iguchi, T. Kozu, L. Liao, K. Okamoto, J. Jones, and J. Kwiatkowski, 2000: Use of the surface reference technique for path attenuation estimates from the TRMM Precipitation Radar. *J. Appl. Meteor.*, **39**, 2053-2070.

Nakamura, K., K. Okamoto, T. Ihara, J. Awaka, and T. Kozu, 1990: Conceptual design of rain radar for the Tropical Rainfall Measuring Mission. *Int. J. Sat. Comm.*, **8**, 257-268.

Nakazawa, T., 1988: Tropical superclusters within intraseasonal variations over the western Pacific. *J. Meteor. Soc. Japan*, **66**, 823-839.

Nakazawa, T., 1995: Intraseasonal oscillations during the TOGA-COARE IOP. *J. Meteor. Soc. Japan*, **73**, 305-319.

Nigam, S., C. Chung, and E. DeWeaver, 2000: ENSO diabatic heating in ECMWF and NCEP-NCAR reanalyses and NCAR CCM3 simulation. *J. Clim.*, **13**, 3152-3171.

Nitta, T., 1977: Response of cumulus updraft and downdraft to GATE A/B-scale motion systems. *J. Atmos. Sci.*, **34**, 1163–1186.

Okamoto, K., J. Awaka, and T. Kozu, 1988: A feasibility study of rain radar for the Tropical Rainfall Measuring Mission. 6: A case study of rain radar system. *J. Comm. Research Lab.*, **35**, 183-208.

Okamoto, K., and T. Kozu, 1993: TRMM Precipitation Radar algorithms. *Proc. IGARSS'93*, IEEE Geoscience and Remote Sensing Society, 426-428.

Okamoto, K., 2003: A short history of the TRMM Precipitation Radar. *AMS Meteorological Monographs: Cloud Systems, Hurricanes, and the Tropical Rainfall Measuring Mission (TRMM) -- A Tribute to Dr. Joanne Simpson*, **29**, 187-195.

Olson, W.S., C.D. Kummerow, Y. Hong, and W.-K. Tao, 1999: Atmospheric latent heating distributions in the tropics derived from passive microwave radiometer measurements. *J. Appl. Meteor.*, **38**, 633-664.

Olson, W.S., C. D. Kummerow, S. Yang, G.W. Petty, W.-K. Tao, T. L. Bell, S.A. Braun, Y. Wang, S.E. Lang, D.E. Johnson, and C. Chiu, 2004: Precipitation and latent heating distributions from satellite passive microwave radiometry. *J. Appl. Meteor.*, in preparation.

Panegrossi, G., S. Dietrich, F.S. Marzano, A. Mugnai, E.A. Smith, X. Xiang, G.J. Tripoli, P.K. Wang, and J.P.V. Poiares Baptista, 1998: Use of cloud model microphysics for passive microwave-based precipitation retrieval: Significance of consistency between model and measurement manifolds. *J. Atmos. Sci.*, **55**, 1644-1673.

Petersen, W.A., S.W. Nesbitt, R.J. Blakeslee, R. Cifelli, P. Hein, and S.A. Rutledge, 2002: TRMM observations of intraseasonal variability in convective regimes over the Amazon. *J. Clim.*, **15**, 1278–1294.

Puri, K., 1987: Some experiments on the use of tropical diabatic heating information for initial state specification. *Mon. Wea. Rev.*, **115**, 1394-1406.

Puri, K., and M. J. Miller, 1990: The use of satellite data in the specification of convective heating for diabatic initialization and moisture adjustment in numerical weather prediction models. *Mon. Wea. Rev.*, **118**, 67-93.

Rajendran, R., T.N. Krishnamurti, V. Misra, and W.-K. Tao, 2004: An empirical cumulus parameterization scheme based on TRMM latent heating profiles. *J. Meteor. Soc. Japan*, **82**, 989-1006..

Raymond, W. H., W. S. Olson, and G. Callan, 1995: Diabatic forcing and initialization with assimilated cloud water and rainwater in a forecast model. *Mon. Wea. Rev.*, **123**, 366-382.

Riehl, H., and J.S. Malkus, 1958: On the heat balance in the equatorial trough zone. *Geophysica*, **6**, 503-538.

Rodgers, E. B., W. S. Olson, V. M. Karyampudi, and H. F. Pierce, 1998: Satellite-derived latent heating distribution and environmental influences in Hurricane Opal (1995). *Mon. Wea. Rev.*, **126**, 1229-1247.

Rodgers, E. B., W. Olson, J. Halverson, J. Simpson, and H. Pierce, 2000: Environmental forcing of supertyphoon Paka's (1997) latent heat structure. *J. Appl. Meteor.*, **39**, 1983-2006.

Rutledge, S.A., R.A. Houze, Jr., M.I. Biggerstaff, and T. Matejka, 1988: The Oklahoma-Kansas mesoscale convective system of 10-11 June 1985: Precipitation structure and single-Doppler radar analysis. *Mon. Wea. Rev.*, **116**, 1409-1430.

Satoh, S., and A. Noda, 2001: Retrieval of latent heating profiles from TRMM radar data. Proceedings of 30th International Conf. on Radar Meteorology, [Munich, Germany; 19-24 July 2001], 340-342.

Schumacher, C., R.A. Houze, Jr., and I. Kraucunas, 2003: The tropical dynamical response to latent heating estimates derived from the TRMM precipitation radar. *J. Atmos. Sci.*, in press.

Shige, S., Y.N. Takayabu, W.-K. Tao, and D.E. Johnson, 2004: Spectral retrieval of latent heating profiles from TRMM PR data. Part I: Development of a model-based algorithm. *J. Appl. Meteor.*, **43**, 1095-1113.

Simpson, J., R.F. Adler, and G. North, 1988: A Proposed Tropical Rainfall Measuring Mission (TRMM) satellite. *Bull. Amer. Meteor. Soc.*, **69**, 278-295.

Simpson, J., C. Kummerow, W.-K. Tao, and R. Adler, 1996: On the Tropical Rainfall Measuring Mission (TRMM). *Meteorol. Atmos. Phys.*, **60**, 19-36.

Simpson, J., and W.-K. Tao, 1993: The Goddard Cumulus Ensemble Model. Part II: Applications for studying cloud precipitating processes and for NASA TRMM. *Terrestrial, Atmospheric and Oceanic Sciences*, **4**, 73-116.

Smith, E.A., 1986: The structure of the Arabian heat low. Part II: Bulk tropospheric heat budget and implications. *Mon. Wea. Rev.*, **114**, 1084-1102.

Smith, E.A., X. Xiang, A. Mugnai, and G. Tripoli, 1992: A cloud radiation model for spaceborne precipitation retrieval. Extended Abstract Vol. of International TRMM Workshop on the Processing and Utilization of the Rainfall Data Measured from Space, Communications Research Laboratory, Tokyo, Japan, 273-283.

Smith, E.A., X. Xiang, A. Mugnai, and G.J. Tripoli, 1994a: Design of an inversion-based precipitation profile retrieval algorithm using an explicit cloud model for initial guess microphysics. *Meteorol. Atmos. Phys.*, **54**, 53-78.

Smith, E.A., A. Mugnai, and G. Tripoli, 1994b: Theoretical foundations and verification of a multispectral, inversion-type microwave precipitation profile retrieval algorithm. In *Passive Microwave Remote Sensing of Land-Atmosphere Interactions* (599-621), VSP Press, Utrecht - The Netherlands, 685 pp.

Smith, E.A., and L. Shi, 1995: Reducing discrepancies in atmospheric heat budget of Tibetan Plateau by satellite-based estimates of radiative cooling and cloud-radiation feedback. *Meteorol. Atmos. Physics*, **56**, 229-260.

Smith, E.A., J. Turk, M. Farrar, A. Mugnai, and X. Xiang, 1997: Estimating 13.8 GHz path integrated attenuation from 10.7 GHz brightness temperatures for TRMM combined PR-TMI precipitation algorithm. *J. Appl. Meteor.*, **36**, 365-388.

Smith, E.A., J. Lamm, R. Adler, J. Alishouse, K. Aonashi, E. Barrett, P. Bauer, W. Berg, A. Chang, R. Ferraro, J. Ferriday, S. Goodman, N. Grody, C. Kidd, D. Kniveton, C. Kummerow, G. Liu, F. Marzano, A. Mugnai, W. Olson, G. Petty, A. Shibata, R. Spencer, F. Wentz, T. Wilheit, and E. Zipser, 1998: Results of WetNet PIP-2 project. *J. Atmos. Sci.*, **55**, 1483-1536.

Smith, E.A., and T.D. Hollis, 2003: Performance evaluation of level 2 TRMM rain profile algorithms by intercomparison and hypothesis testing. *AMS Meteorological Monographs: Cloud Systems, Hurricanes, and the Tropical Rainfall Measuring Mission (TRMM) -- A Tribute to Dr. Joanne Simpson*, **29**, 207-222.

Smith, E.A., P. Bauer, F.S. Marzano, C.D. Kummerow, D. McKague, A. Mugnai, and G. Panegrossi, 2002: Intercomparison of microwave radiative transfer models in precipitating clouds. *IEEE Trans. Geosci. Rem. Sens.*, **40**, 541-549.

Soong, S.-T., and W.-K. Tao, 1980: Response of deep tropical clouds to mesoscale processes. *J. Atmos. Sci.*, **37**, 2016-2036.

Soong, S.-T., and W.-K. Tao, 1984: A numerical study of the vertical transport of momentum in a tropical rainband. *J. Atmos. Sci.*, **41**, 1049-1061.

Stokes, G.M., and S.E. Schwartz, 1994: The Atmospheric Radiation Measurement (ARM) Program: Programmatic background and design of the Cloud and Radiation Test Bed. *Bull. Amer. Meteor. Soc.*, **75**, 1201–1222.

Sui, C.-H., and K.-M. Lau, 1988: Origin of low-frequency (intraseasonal) oscillations in the tropical atmosphere. Part II: Structure and propagation of mobile wave-CISK modes and their modification by lower boundary forcings. *J. Atmos. Sci.*, **46**, 37-56.

Sumi, A., and T. Nakazawa, 2002: Satellite monitoring for the season-to-interannual climate fluctuations. *Korean J. Atmos. Sci.*, **5S**, 13-28.

Takayabu, Y.N., K.-M. Lau, and C.-H. Sui, 1996: Observation of a quasi two-day wave during TOGA-COARE. *Mon. Wea. Rev.*, **124**, 1892-1913.

Takayabu, Y.N., 2002: Spectral representation of rain features and diurnal variations observed with TRMM PR over the equatorial areas. *Geophys. Res. Let.*, **29**, 301-304.

Tao, W.-K., and S.-T. Soong, 1986: A study of the response of deep tropical clouds to mesoscale processes: Three-dimensional numerical experiments. *J. Atmos. Sci.*, **43**, 2653-2676.

Tao, W.-K., J. Simpson, and S.-T. Soong, 1987: Statistical properties of a cloud ensemble: A numerical study. *J. Atmos. Sci.*, **44**, 3175-3187.

Tao, W.-K., J. Simpson, S. Lang, M. McCumber, R. Adler, and R. Penc, 1990: An algorithm to estimate the heating budget from vertical hydrometeor profiles. *J. Appl. Meteor.*, **29**, 1232-1244.

Tao, W.-K., and J. Simpson, 1993: The Goddard Cumulus Ensemble Model. Part I: Model description. *Terrestrial, Atmospheric and Oceanic Sciences*, **4**, 19-54.

Tao, W.-K., J. Simpson, C.-H. Sui, B. Ferrier, S. Lang, J. Scala, M.-D. Chou, and K. Pickering, 1993a: Heating, moisture and water budgets of tropical and mid-latitude squall lines: Comparisons and sensitivity to longwave radiation. *J. Atmos. Sci.*, **50**, 673-690.

Tao, W.-K., S. Lang, J. Simpson, and R. Adler, 1993b: Retrieval algorithms for estimating the vertical profiles of latent heat release: Their applications for TRMM. *J. Meteor. Soc. Japan*, **71**, 685-700.

Tao, W.-K., J. Scala, B. Ferrier, and J. Simpson, 1995: The effects of melting processes on the development of a tropical and a mid-latitudes squall line. *J. Atmos. Sci.*, **52**, 1934-1948.

Tao, W.-K., J. Simpson, S. Lang, C.-H. Sui, B. Ferrier, and M.-D. Chou, 1996: Mechanisms of cloud-radiation interaction in the tropics and mid-latitudes. *J. Atmos. Sci* ., **53**, 2624-2651.

Tao, W.-K., S. Lang, J. Simpson, W.S. Olson, D. Johnson, B. Ferrier, C. Kummerow, and R. Adler, 2000: Retrieving vertical profiles of latent heat release in TOGA COARE convective systems using a cloud resolving model, SSM/I and radar data. *J. Meteor. Soc. Japan,* **78**, 333-355.

Tao, W.-K., S. Lang, W.S. Olson, S. Yang, R. Meneghini, J. Simpson, C. Kummerow, E. Smith and J. Halverson, 2001: Retrieved vertical profiles of latent heating release using TRMM rainfall products for February 1998. *J. Appl. Meteor.*, **40**, 957-982.

Tao, W.-K., 2003: Goddard Cumulus Ensemble (GCE) Model: Application for understanding precipitation processes. *AMS Meteorological Monographs: Cloud Systems, Hurricanes, and the Tropical Rainfall Measuring Mission (TRMM) -- A Tribute to Dr. Joanne Simpson*, **29**, 107-138.

Tao, W.-K., J. Simpson, D. Baker, S. Braun, M.D. Chou, B. Ferrier, D. Johson, A. Khain, S. Lang, B. Lynn, C.-L Shie, D. Starr, Y. Wang, and P. Wetzel, 2003a: Microphysics, radiation and surface processes in the Goddard Cumulus Ensemble (GEC) model. *Meteorol. Atmos. Phys.*, **82**, 97-137.

Tao, W.-K., C.-L. Shie, R. Johnson, S. Braun, J. Simpson, and P.E. Ciesielski, 2003b: Convective systems over the South China Sea: Cloud resolving model simulations. *J. Atmos. Sci.,* **60**, 2929-2956.

Tripoli, G.J., 1992a: A nonhydrostatic mesoscale model designed to simulate scale interaction. *Mon. Wea. Rev.*, **120**, 1342-1359.

Tripoli, G.J., 1992b: An explicit three-dimensional nonhydrostatic simulation of a tropical cyclone. *Meteorol. Atmos. Phys.*, **49**, 229-254.

Tripoli, G.J., 2004: A scalable nonhydrostatic model featuring variably stepped topography. Part 1: Formulation and evaluation of performance on simple obstacle flow problems. *Mon. Wea. Rev.*, submitted.

Vijaya Kumar, T. S. V., T.N. Krishnamurti, M. Fiorino, and M. Nagata, 2003: Multimodel superensemble forecasting of tropical cyclones in the Pacific. *Mon. Wea. Rev.*, **131**, 574–583.

Wang, W., and T. T. Warner, 1988: Use of four-dimensional data assimilation by Newtonian relaxation and latent-heat forcing to improve a mesoscale-model precipitation forecast: A case study. *Mon. Wea. Rev.*, **116**, 2593-2613.

Wang, Y., W.-K. Tao, and J. Simpson, 1996: The impact of ocean surface fluxes on a TOGA COARE convective system. *Mon. Wea. Rev.*, **124**, 2753–2763.

Webster, P.J., and R.A. Houze Jr., 1991: The Equatorial Mesoscale Experiment (EMEX): An overview. *Bull. Amer. Meteor. Soc.*, **72**, 1481-1506.

Webster, P.J., and R. Lukas, 1992: TOGA-COARE: The coupled ocean-atmosphere response experiment. *Bull. Amer. Meteor. Soc.*, **73**, 1377-1416.

Wilheit, T.T., J.S. Theon, W.E. Shenk, L.J. Allison, and E.B. Rodgers, 1976: Meteorological interpretations of the images from the Nimbus 5 Electrically Scanned Microwave Radiometer. *J. Appl. Meteor.*, **15**, 166–172.

Williford, E.C., T.N. Krishnamurti, R. Correa-Torres, S. Cocke, Z. Christidis, and T.S.V. Vijaya Kumar, 2003: Real-time multimodel superensemble forecasts of Atlantic tropical systems of 1999. *Mon. Wea. Rev.*, **131**, 1878–1894.

Yanai, M., S. Esbensen, and J. Chu, 1973: Determination of average bulk properties of tropical cloud clusters from large-scale heat and moisture budgets. *J. Atmos. Sci.*, **30**, 611-627.

Yanai, M., B. Chen, W.-W. Tung, 2000: The Madden-Julian oscillation observed during the TOGA COARE IOP: Global view. *J. Atmos. Sci.*, **57**, 2374-2396.

Yang, S., and E.A. Smith, 1999a: Moisture budget analysis of TOGA-COARE area using SSM/I retrieved latent heating and large scale Q_2 estimates. *J. Atmos. Oceanic Technol.*, **16**, 633-655.

Yang, S., and E.A. Smith, 1999b: Four dimensional structure of monthly latent heating derived from SSM/I satellite measurements. *J. Clim.*, **12**, 1016-1037.

Yang, S., and E.A. Smith, 2000: Vertical structure and transient behavior of convective-stratiform heating in TOGA-COARE from combined satellite-sounding analysis. *J. Appl. Meteor.*, **39**, 1491-1513.

Yang, S., W. S. Olson, J.-J. Wang, T. L. Bell, E. A. Smith, and C. D. Kummerow, 2004: Precipitation and latent heating distributions from satellite passive microwave radiometry. Part II: Evaluation of estimates using independent data. *J. Appl. Meteor.*, in preparation.

Yang, S., 2004: Precipitation and latent heating estimation from passive microwave satellite measurements: A review. *Observations, Theory, and Modeling of the Atmospheric and Oceanic Variability*, World Scientific Series on Meteorology of East Asia, **Vol. 3**, World Scientific Publishing Co. Pte. Ltd., Singapore, 484-500.

Yang, S., and E.A. Smith, 2004: Mechanisms for diurnal variability of global tropical rainfall observed from TRMM. *J. Clim.*, submitted.

Yun, W.T., L. Stefanova, and T.N. Krishnamurti, 2003: Improvement of the multimodel superensemble technique for seasonal forecasts. *J. Clim.*, **16**, 3834–3840.

Yuter, S.E., R.A. Houze, Jr., E.A. Smith, T.T. Wilheit, and E. Zipser, 2004: An overview of the 1999 TRMM Kwajalein Experiment (KWAJEX). *J. Appl. Meteor.*, in press.

List of Tables

Table 1: Summary of CSH, GPROF Heating, HH, PRH, and SLH latent heating retrieval algorithms, in which key references, essential algorithm input parameters, past case studies, and relevant space-time resolutions of heating calculations are provided. [Wherever + symbols precede citations in "References" column, corresponding + symbols in other columns denote associated information vis-à-vis those citations. In "Alg" column, "RECON" indicates Reconstruction and "COMB" indicates Combined, while in "Resolution" column, *inst* indicates instantaneous, *hr* indicates 1 hour, *dy* indicates 1 day, and *mo* indicates 1 month.]

Alg	References	Input Parameters	Cases	Resolution
CSH (RECON; SSM/I)	Tao *et al.* (1993b)	▪ surface rain rate ▪ conv / strat fractions	▪ GATE (1974), ▪ PRE-STORM (1985) ▪ Trop Cyclone Thelma'87	200 - 300 *km*; *dy*
CSH (RECON; PR)	+ Tao *et al.* (2000) + Tao *et al.* (2001) + Tao *et al.* (this study)	+ surface rain rate & conv / strat fractions + CSH, GPROF, & HH algorithms + surface rain rate & conv / strat fractions	+ TOGA-COARE (1992-93) + Various Tropical Regimes (Feb'98) + Global Tropics (Dec'97-Nov'00)	+ 500 *km*; 3-6 *hr* + 110 *km*; *dy* + 55 *km*; *mo*
GPROF (SSM/I)	+Olson *et al.* (1999) +Olson *et al.* (1999)	• microwave radiance observations ▪ cloud-model generated latent heat profiles / microwave radiance simulations	+ Hurricane Andrew (1992) + Tropical MCS's (1992) + TOGA-COARE (1992-93)	+ 25 *km*; *inst* + 25 *km*; *inst* + 500 *km*; *dy*
HH (RECON)	Tao *et al.* (1990, 1993b) Simpson and Tao (1993)	▪ surface rain rate for all precip categories ▪ hydrometeor profiles (cld / rain / ice crystal / snow / graupel) ▪ terminal velocities of rain / snow / graupel hydrometeors	▪ GATE (1974) ▪ PRE-STORM (1985) ▪ EMEX (1987)	+ 15 *km*; *inst* + 15 *km*; *inst* + 15-50 *km*; *inst* + 275 *km*; *mo* + *5 km; inst*
HH (SSM/I; PR;TMI; COMB)	+ Smith *et al.* (1992, 1994a) + Smith *et al.* (1994a, 1994b) + Yang & Smith (1999a, 2000) + Yang & Smith (1999b) + YS'00 in Tao *et al.* (this study)	▪ hydrometeor profiles (cld / rain / snow / aggregate / graupel) ▪ terminal velocities of rain / snow / aggregate / graupel hydrometeors ▪ cld vertical velocities	+ Trop Cyclones Thelma'87/Hugo'89 + TOGA-COARE (1992-93) + TOGA-COARE (1992-93) + Global Tropics (1992) + Hurricane Bonnie'98	5-100 *km; inst*
PRH (PR)	Satoh & Noda (2001)	▪ surface rain rate for all precip categories ▪ terminal velocities of rain hydrometeors ▪ cld vertical velocities ▪ precip top / bright band / cld base heights	▪ Squall line in Oklahoma	*5-100 km; inst*
SLH (RECON)	Shige *et al.* (2004)	▪ surface rain rate for all precip categories ▪ conv / strat / anvil index ▪ rain rates at & heights of melting level / precip top	▪ TOGA-COARE (1992-93)	*5-100 km; inst*

Table 2: General strengths and weaknesses of CSH, GPROF Heating, HH, PRH, and SLH latent heating retrieval algorithms.

Alg	General Strengths	General Weaknesses
CSH	▪ CRM model-based and robust algorithm with long history. ▪ Adaptable to any TRMM level-2 algorithm (PR, TMI, COMB). ▪ Adheres to convective/stratiform heating variational characteristics based on diagnostic budget studies. ▪ Extensive simulation and Q_1 validation studies involving field campaign datasets from GATE, EMEX, PRE-STORM, TOGA COARE, SCSMEX, TRMM-LBA, KWAJEX, and DOE-ARM Program.	▪ Restricted to convective/stratiform categories and sensitive to errors in corresponding cover fractions. ▪ Imperfections and incompleteness in CRM-generated heating profiles defined in look-up table lead to systematic errors in retrieved profiles. ▪ Zero surface rainfall leads to zero latent heating aloft.
GPROF Heating	▪ CRM model-based in which diagnosed latent heating profiles consistent with associated retrieved rain parameters. ▪ Random error of retrieved parameters well defined because of Bayesian framework. ▪ Heating profiles retrieved at TMI footprint scale (~14 km).	▪ Rainfall and latent heating may have different temporal scales. ▪ Errors in cloud/radiative model database simulations lead to systematic errors in retrieved heating profiles. ▪ Under-representation of observed precipitation and latent heating structures in cloud/radiative model database leads to errors in heating estimates.
HH	▪ Physically based and direct microphysics approach with long history. ▪ Adaptable to any TRMM level-2 algorithm (PR, TMI, COMB). ▪ Latent heating closely related to vertical precipitation rate gradients -- accurate precipitation mass flux inputs result in small systematic errors. ▪ Heating profiles retrieved at either PR or TMI footprint scales (~5 or ~14 km, respectively) or area-averaged scales.	▪ Sensitive to noise in retrieved precipitation profiles, i.e., noise in hydrometeor or rain rate profiles passed on to heating profiles. ▪ Uncertainty generated with knowledge of cloud-scale vertical motion -- must be assumed zero if unknown. ▪ Uncertainty generated from errors in formulation of hydrometeor terminal velocities -- more so at upper levels.
PRH	▪ Produces distinct heating structures for various types of organized precipitation systems (e.g., squall lines, tropical cyclones, MCSs). ▪ Differentiated cloud vertical velocities provided for convective, stratiform, and deep anvil precipitation categories. ▪ Heating profiles retrievable at instantaneous scale.	▪ Sensitive to estimated vertical velocities and hydrometeor profiles -- especially for mixed phase. ▪ Uses idealized thermodynamic assumptions, and may produce cooling near cloud top and in upper part of cloud. ▪ Limited sampling due to PR's narrow swath width.
SLH	▪ Differentiates heating structures between shallow-convective and deep-convective stages. ▪ Produces heating for decaying anvil stage even with zero surface rainfall. ▪ Heating profiles retrievable at instantaneous scale.	▪ Restricted to convective/shallow-stratiform/anvil stratus categories and sensitive to errors in corresponding cover fractions. ▪ Imperfections and incompleteness in CRM-generated heating profiles defined in look-up table lead to systematic errors in retrieved profiles. ▪ Limited sampling due to PR's narrow swath width.

List of Figures

Cover Figure: Five-year mean $Q1$ heating rates at 8, 5, and 2 km AGL (upper 3 panels) along with surface rain rates (lower panel) over global tropics determined by Goddard Space Flight Center (GSFC) Convective-Stratiform Heating (CSH) algorithm applied to 1998-2002 Precipitation Radar (PR) measurements acquired from Tropical Rainfall Measuring Mission (TRMM) satellite. [See related article by Tao *et al.*]

Figure 1: Height-length cross-sections of GCE-CRM generated LH (°C day^{-1}) consisting of sum of heating by condensation, freezing, and deposition, and cooling by evaporation, melting, and sublimation -- associated with mid-latitude continental (PRE-STORM) squall line (upper panel) and tropical ocean (TOGA-COARE) MCS (lower panel). [Discussions of simulations are in Tao *et al.* (1993a, 1995, 1996), Wang *et al.* (1996), Lang *et al.* (2003).]

Figure 2: Evolution of apparent heat source profile ($Q1$) averaged over TOGA-COARE IFA for 8-day period (19-27 December 1992) -- derived diagnostically every 6 hours by Lin and Johnson (1996) (upper panel) and simulated every 2 minutes by GCE-CRM (lower panel). [Contour interval is 5°C day^{-1}.]

Figure 3: Upper panel shows plan view of near-surface rain rates for Hurricane Bonnie (22 August 1998) retrieved from TRMM PR/TMI Combined algorithm; middle panel shows vertical nadir cross-section of along-track rain rate profiles; and lower panel shows vertical nadir cross-section of along-track LH profiles from HH algorithm.

Figure 4: ULH and URH panels show TMI-retrieved surface and convective rain rates from GPROF rain algorithm- for squall line in North Atlantic Ocean on 7 April 1998. Lower panel shows height-length cross-section (~28-km horizontal resolution) of total precipitation water content (color shading in g m^{-3}) and $Q1$-QR diabatic heating (contours in °C h^{-1}) from GPROF Heating algorithm.

Figure 5a: Five panels of upper diagram show latent heating analysis for tropical Pacific Typhoon Jelawat in developing stage (2 August 2000) in which arrows indicate location of eye, while five panels of lower diagram show identical analysis for MCS over tropical ocean north-west of Australia (16 February 1998). For each of two diagrams, ULH, MLH, and LLH panels show height-scan cross-section of PR-retrieved rain rate profile (mm h^{-1}), along with SLH-generated and PRH-generated LH profiles (°C h^{-1}), respectively. Two pairs of URH and LRH panels show area-mean vertical profiles of both SLH-generated $Q1$-QR (red) and LH (black), plus PRH-generated LH (black), all in °C h^{-1}.

Figure 5b: Four panels of diagram show latent heating analysis for mid-latitude Oklahoma squall line (10 May 1999). ULH, MLH, and LLH panels show height-scan cross-sections of TRMM-PR-observed radar reflectivity profile (ZE in dBZ), PR-retrieved rain rate profile (mm h^{-1}), and PRH-generated LH profile (°C h^{-1}), respectively. LRH panel shows area-mean vertical profile of PRH-generated LH in °C h^{-1}.

Figure 6: Five-year (1998-2002) mean Q_1 profiles estimated from CSH algorithm for spring, summer, autumn, and winter over entire tropics (left panel), continental tropics (middle panel), and oceanic tropics (right panel) -- all based on TRMM-PR retrievals.

Figure 7: TRMM-PR-based Q_1 heating anomalies at 8 km AGL for El Niño episode during DJF 1997-98 (ULH panel) and La Niña episode during DJF 1998-99 (LLH panel) -- generated by CSH algorithm. Average 3-year (1997-99), 3-month El Niño episode, and 3-month La Niña episode heating and heating-anomaly profile pairs over entire tropics are shown in right-hand panel in black, red, and blue, respectively.

Figure 8: Evolution of Q_1 profile reconstructed from GCE-CRM simulation by CSH algorithm averaged over TOGA-COARE IFA for 8-day period (19-27 December 1992) -- compare to results in Fig. 2. Reconstruction uses CRM parameters retrievable from PR data as input (i.e., surface rain rate and convective/stratiform fractions). [Contour interval is 5°C day^{-1}.]

Figure 9: Evolution of LH profile (5-min time-step) from: GCE-CRM simulation (upper panel), SLH algorithm reconstruction (middle panel), and CSH algorithm reconstruction (lower panel), averaged over TOGA-COARE IFA for 8-day period (19-27 December 1992). Contour interval is 5°C day^{-1}. GCE-CRM simulated convective/shallow-stratiform/anvil stratus fractions, surface rain rates, PTHs, and melting level rain rates are used as inputs to SLH scheme with profiles averaged over 512 x 512 km grid mesh. [From Shige et al. 2004.]

Figure 10: Cloud model simulation of GATE vertical profiles of heating rate by condensation (c), evaporation (e), vertical eddy heat flux convergence ($\pi[\partial \overline{w'\theta'}/\partial z]$), and cloud partition of apparent heating ($Q_1[cld]$) -- along with diagnostic calculations of Q_1 - Q_R (using radiosonde data), all in units of °C hr^{-1}. [From Tao and Soong (1986).]

Figure 11: Three left-most pairs of diagrams illustrate isometric projections of volume hydrometeor distributions (upper panels) and plan-view surface rain rates (lower panels) for instantaneous realizations from GCE-CRM simulations of SCSMEX, KWAJEX, and DOE-ARM MCS storm cases. Upper panel iso-surface color scheme assigns white for cloud droplets and ice crystals, blue for snow, red for graupel and hail, and green for rain. Right-most pair of diagrams illustrate near-surface, forward-modeled radar reflectivities for TRMM-LBA easterly regime (upper panel) and westerly regime (lower panel) MCS cases, also based on GCE-CRM simulations.

Figure 12a: KWAJEX rainfall time series consisting of measured and modeled rain rates. Both KPOL-Radar measurements and TRMM-PR retrievals are given for entire IOP, while GCE-CRM simulated estimates are provided from Aug 29 through Sep 12 (both 2D and 3D CRM designs are used to provide simulated rainfall). [Top diagram from Yuter et al. (2004).]

Figure 12b: KWAJEX heat budget time series consisting of diagnostically-calculated and GCE-CRM-simulated Q_1 profiles for three different time sequences during IOP (upper, middle, lower panel pairs illustrate 5-, 3-, 15-day time series, respectively). Green and red contours indicate positive and negative Q_1 regions, respectively.

Figure 13: $Q1$ profiles from diagnostic calculations (Johnson and Ciesielski 2002), GCE-CRM simulation, PR-based CSH algorithm, and TMI-based GPROF algorithm averaged over ~6 x 10 deg lat-lon box designated as SCSMEX-NESA for 37-day period (15 May - 20 June 1998). Two sets of look-up-table profiles are used with GCE-CRM and CSH algorithm representing conditions for: (1) South China Sea (scs), and (2) general tropical ocean (gto). Color insert is isometric rendition of GCE model simulation for 24 May 1998, where white, blue, red, and green iso-surfaces denote cloud droplets - ice crystals, snow, graupel - hail, and rain, respectively. [Most surface rainfall is produced by melting graupel.]

Figure 14: GPCP precipitation for 8 February 1998 representing blend of satellite retrievals and rain gauge observations (upper panel), Florida State University global spectral model (FSU-GSM) day-2 forecast from ECPS experiment (middle panel), and FSU-GSM day-2 forecast from control experiment (lower panel). [From Rajendran *et al.* 2004.]

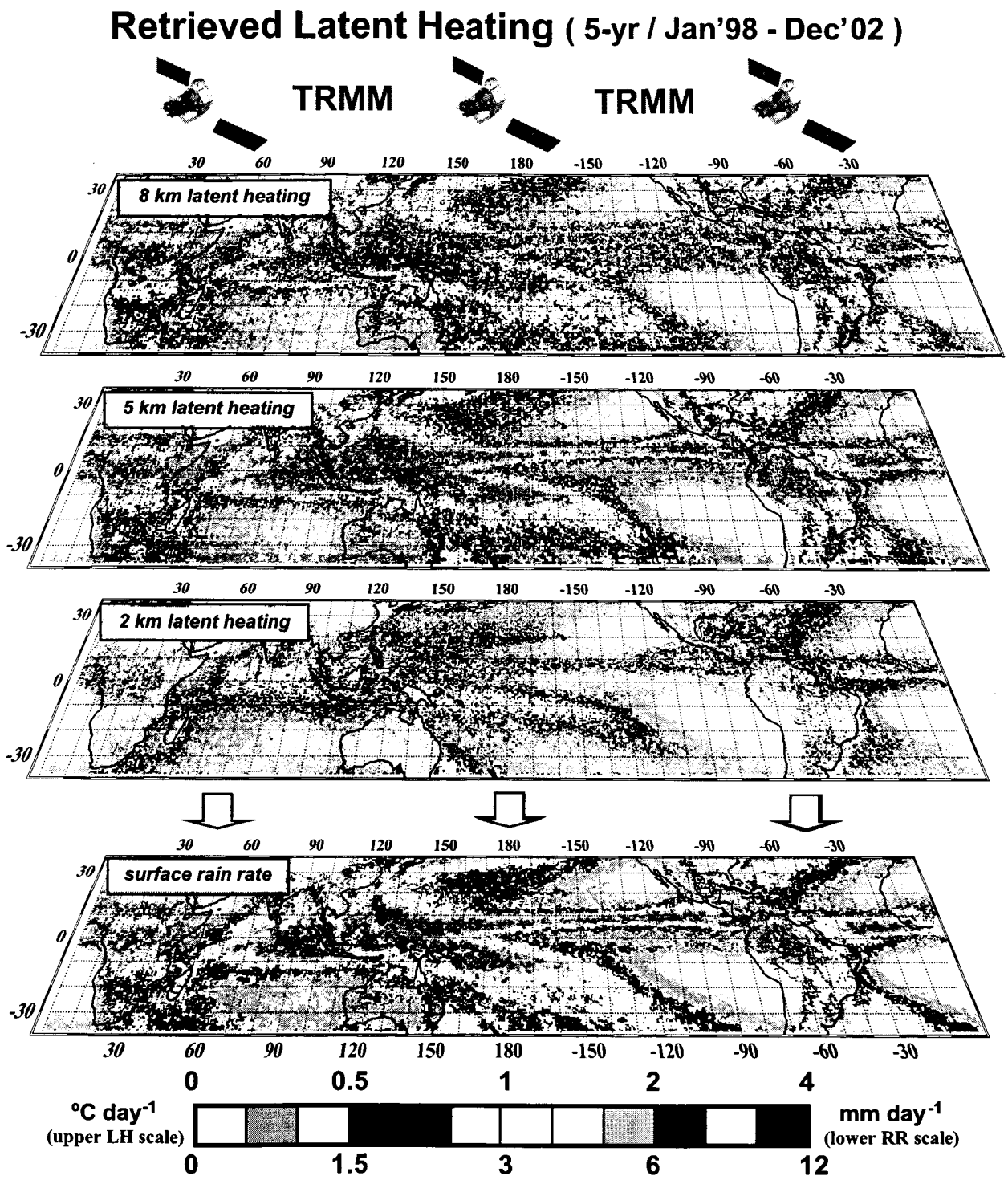

Cover Figure: Five-year mean Q_1 heating rates at 8, 5, and 2 km AGL (upper 3 panels) along with surface rain rates (lower panel) over global tropics determined by Goddard Space Flight Center (GSFC) Convective-Stratiform Heating (CSH) algorithm applied to 1998-2002 Precipitation Radar (PR) measurements acquired from Tropical Rainfall Measuring Mission (TRMM) satellite. [See related article by Tao *et al.*]

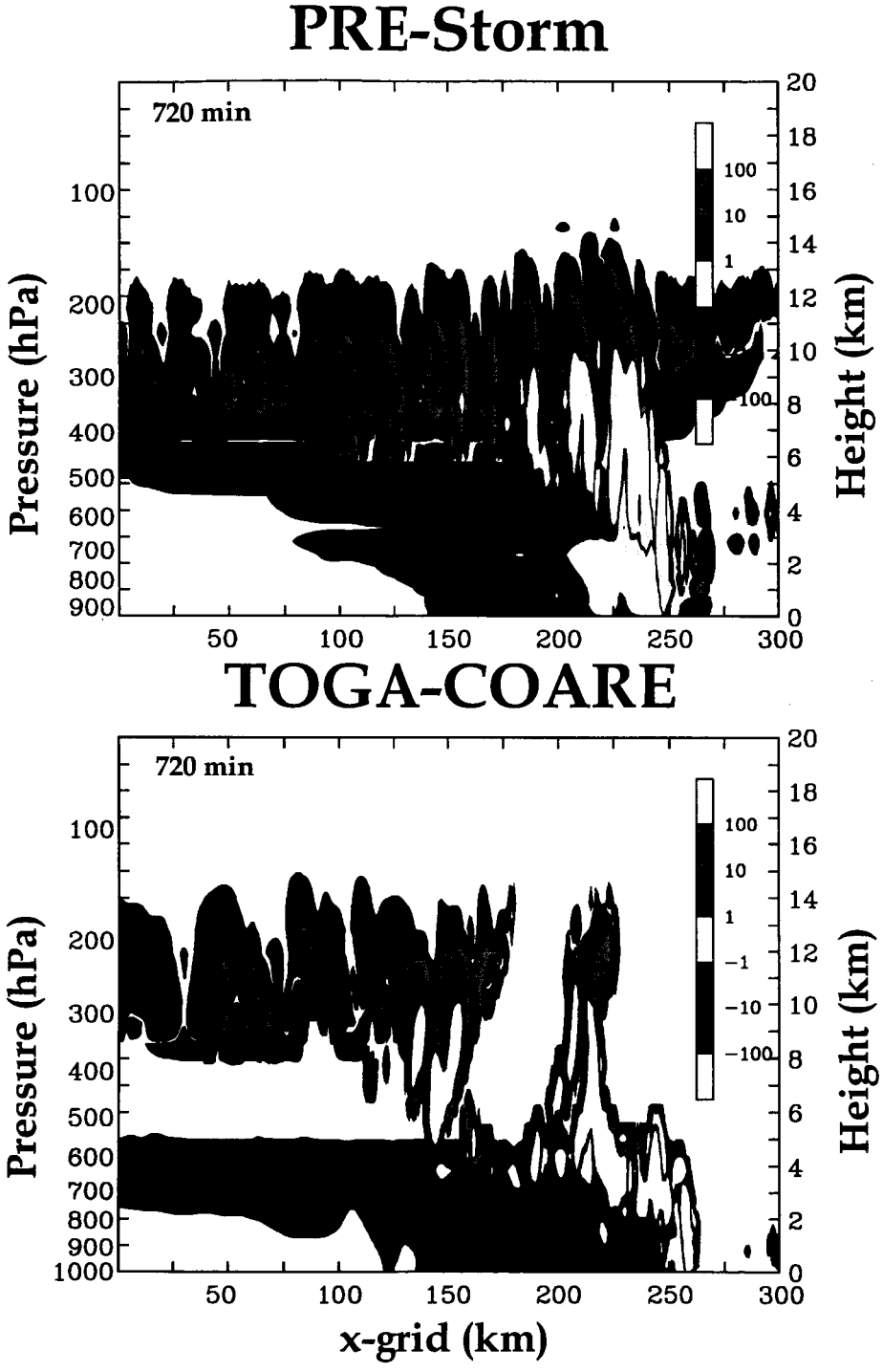

Figure 1: Height-length cross-sections of GCE-CRM generated LH (°C day^{-1}) consisting of sum of heating by condensation, freezing, and deposition, and cooling by evaporation, melting, and sublimation -- associated with mid-latitude continental (PRE-STORM) squall line (upper panel) and tropical ocean (TOGA-COARE) MCS (lower panel). [Discussions of simulations are in Tao *et al.* (1993a, 1995, 1996), Wang *et al.* (1996), Lang *et al.* (2003).]

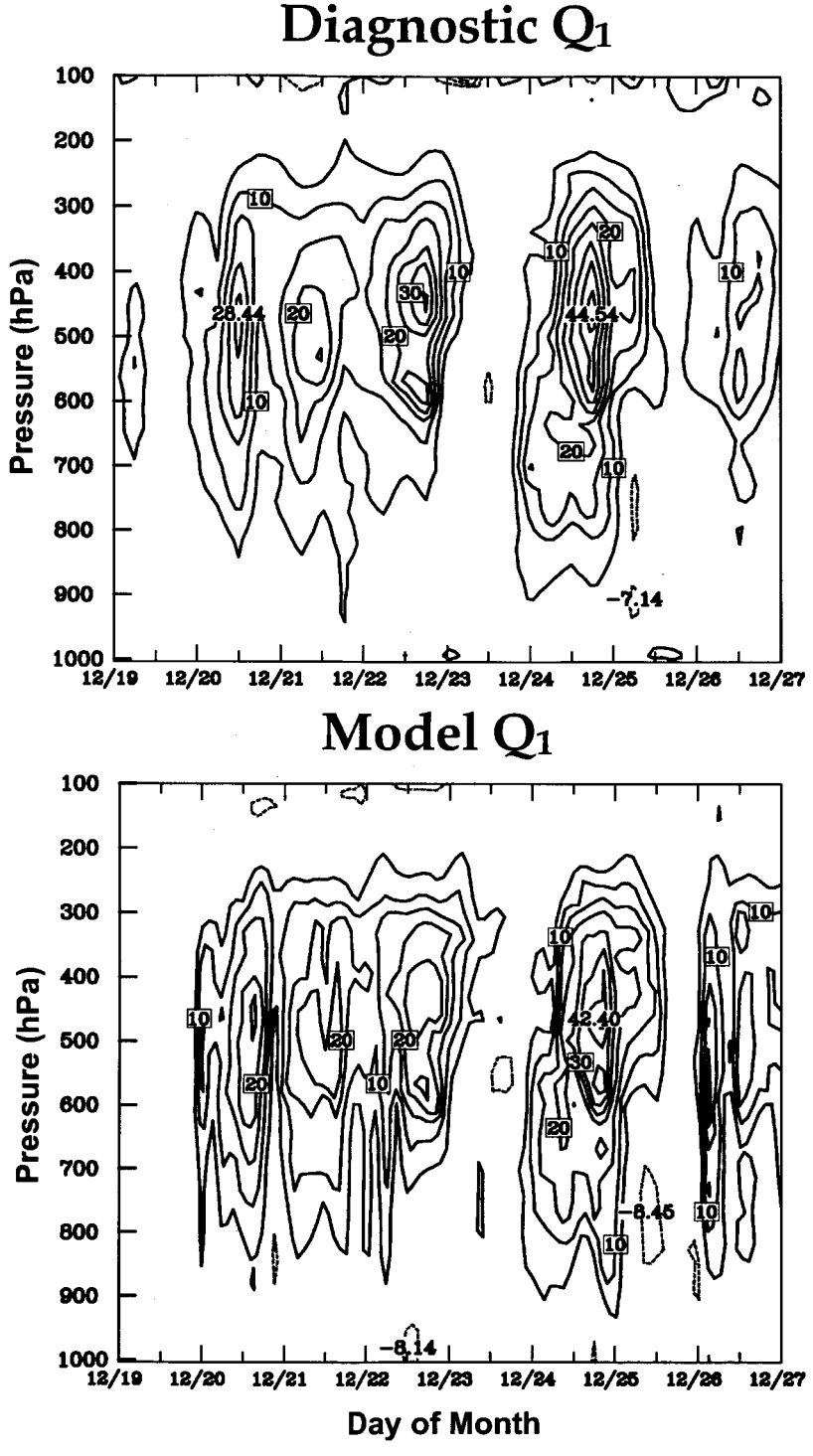

Figure 2: Evolution of apparent heat source profile (*Q1*) averaged over TOGA-COARE IFA for 8-day period (19-27 December 1992) -- derived diagnostically every 6 hours by Lin and Johnson (1996) (upper panel) and simulated every 2 minutes by GCE-CRM (lower panel). [Contour interval is 5°C day^{-1}.]

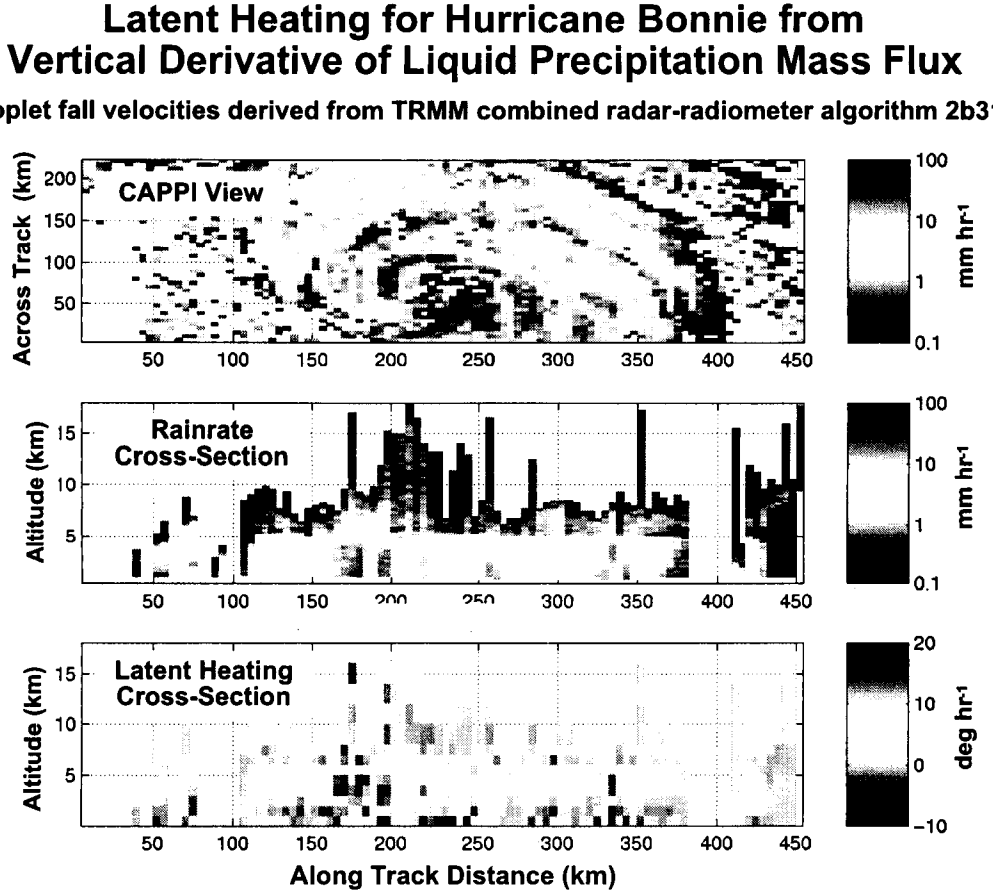

$$R^{*}_{rd}(z) = -\left[\overline{W}_{rd}(z) + \overline{W}(z)\right] \bullet LWC_{rd}(z)$$

$$R^{*}_{ip}(z) = -\left[\overline{W}_{ip}(z) + \overline{W}(z)\right] \bullet IWC_{ip}(z)$$

latent heat profile (Q) due to condensation and deposition heating

$$Q(z) = \frac{g}{c_p} \bullet \left[L_v \bullet \frac{\partial R^{*}_{rd}(z)}{\partial p} + (\delta_{l,j} L_v + L_f) \bullet \frac{\partial R^{*}_{ip}(z)}{\partial p} \right]$$

j = 1 above melting level
= 0 below melting level

Figure 3: Upper panel shows plan view of near-surface rain rates for Hurricane Bonnie (22 August 1998) retrieved from TRMM PR/TMI Combined algorithm; middle panel shows vertical nadir cross-section of along-track rain rate profiles; and lower panel shows vertical nadir cross-section of along-track LH profiles from HH algorithm.

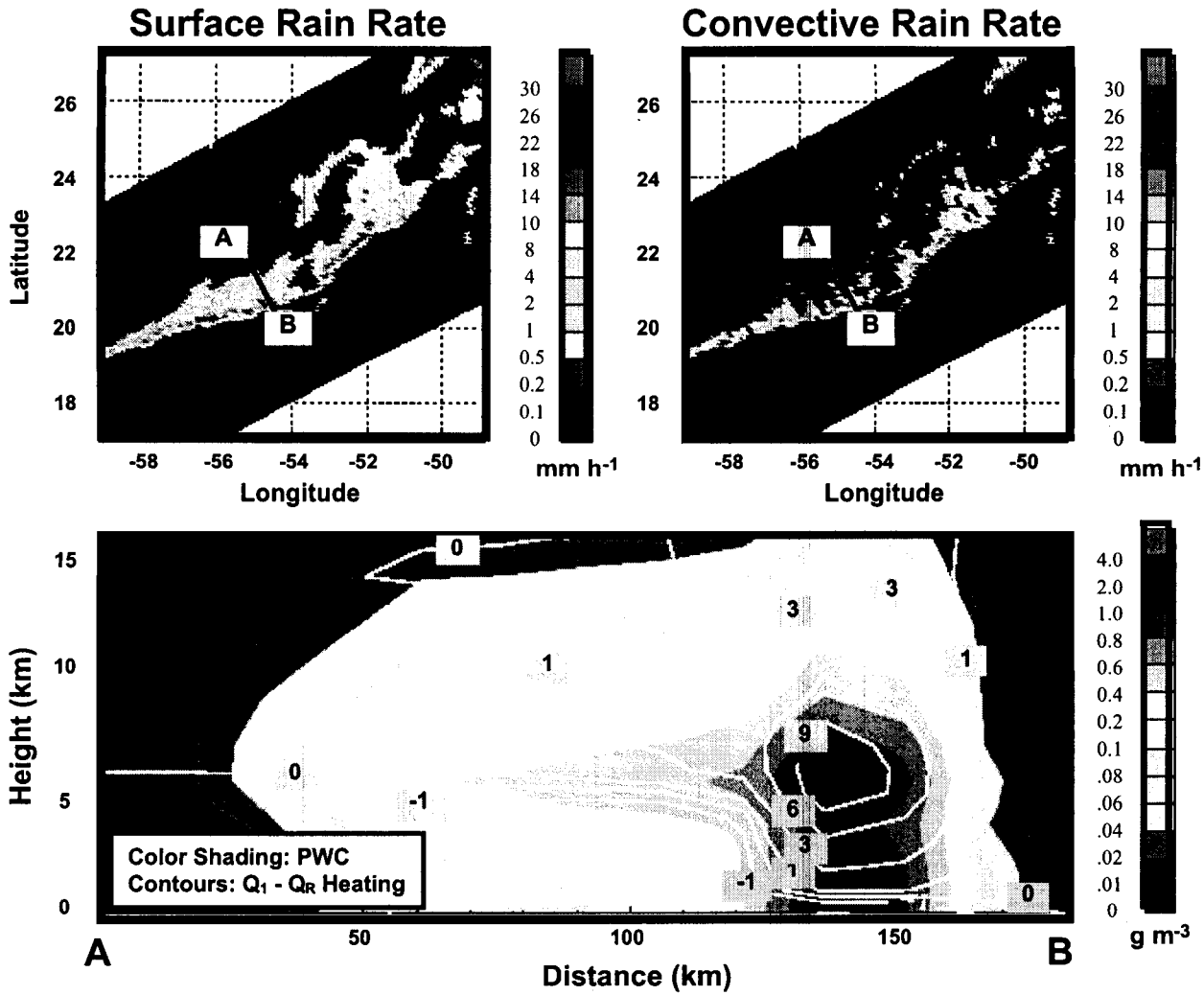

Figure 4: ULH and URH panels show TMI-retrieved surface and convective rain rates from GPROF rain algorithm- for squall line in North Atlantic Ocean on 7 April 1998. Lower panel shows height-length cross-section (~28-km horizontal resolution) of total precipitating water content (color shading in g m^{-3}) and $Q1$-QR diabatic heating (contours in °C h^{-1}) from GPROF Heating algorithm.

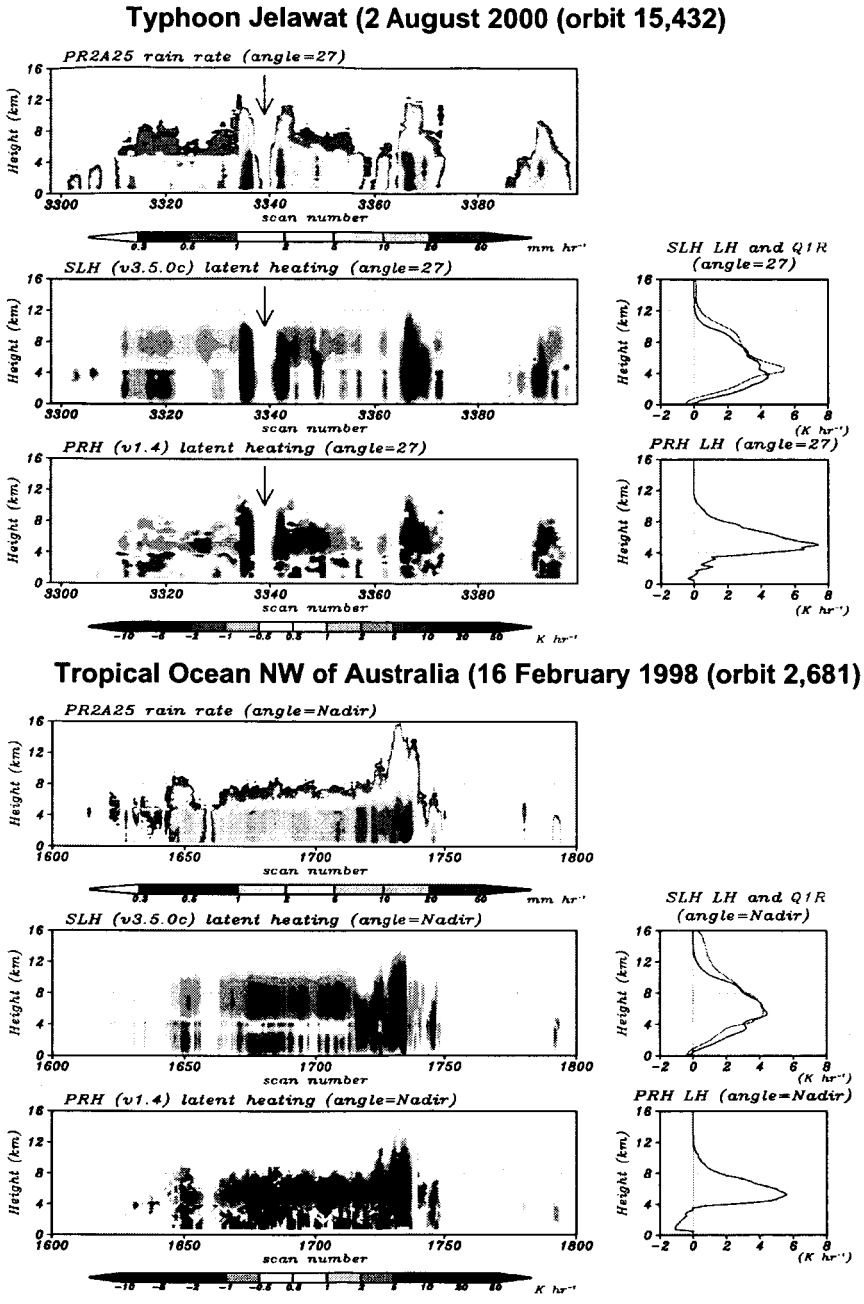

Figure 5a: Five panels of upper diagram show latent heating analysis for tropical Pacific Typhoon Jelawat in developing stage (2 August 2000) in which arrows indicate location of eye, while five panels of lower diagram show identical analysis for MCS over tropical ocean north-west of Australia (16 February 1998). For each of two diagrams, ULH, MLH, and LLH panels show height-scan cross-section of PR-retrieved rain rate profile (mm h^{-1}), along with SLH-generated and PRH-generated LH profiles (°C h^{-1}), respectively. Two pairs of URH and LRH panels show area-mean vertical profiles of both SLH-generated $Q1$-QR (red) and LH (black), plus PRH-generated LH (black), all in °C h^{-1}.

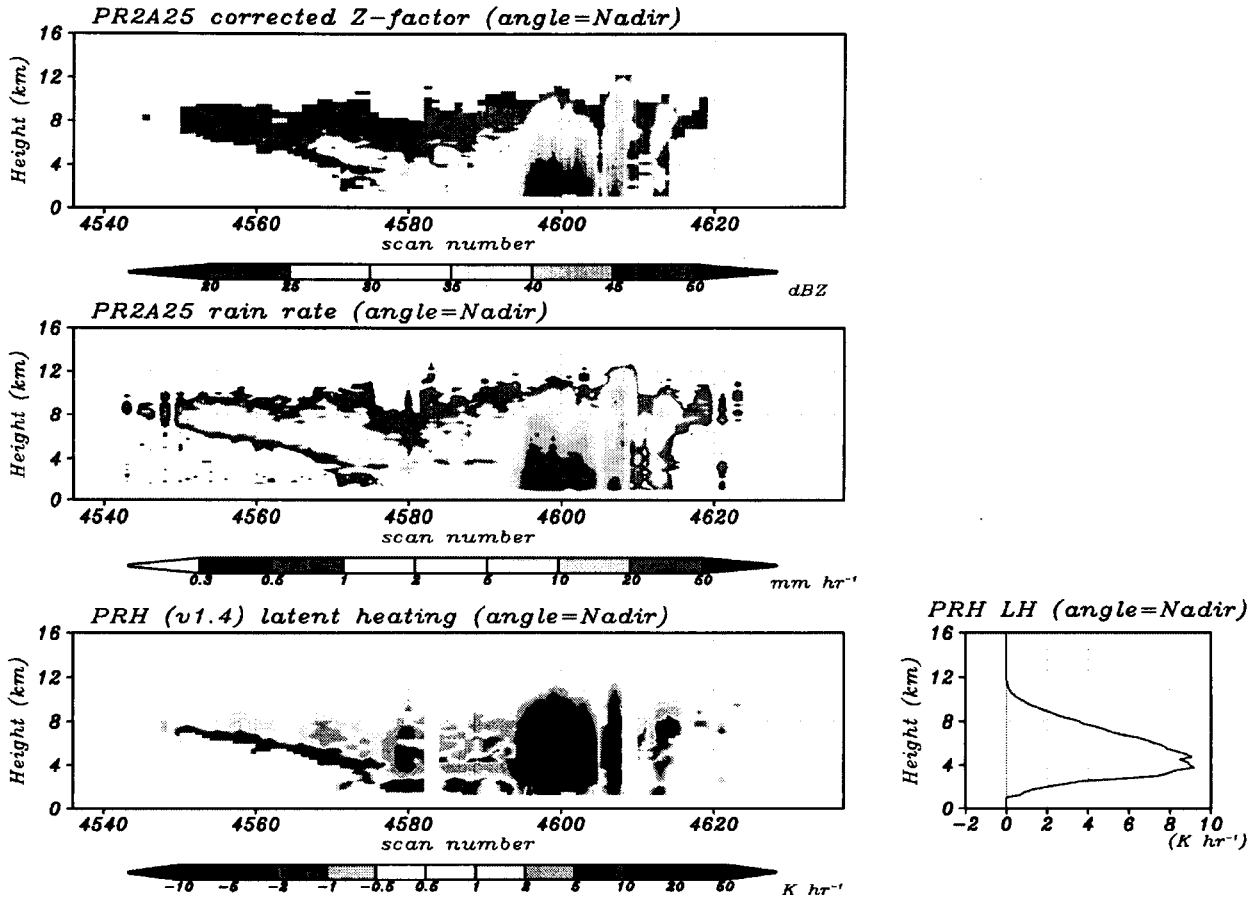

Figure 5b: Four panels of diagram show latent heating analysis for mid-latitude Oklahoma squall line (10 May 1999). ULH, MLH, and LLH panels show height-scan cross-sections of TRMM-PR-observed radar reflectivity profile (ZE in dBZ), PR-retrieved rain rate profile (mm h^{-1}), and PRH-generated LH profile (°C h^{-1}), respectively. LRH panel shows area-mean vertical profile of PRH-generated LH in °C h^{-1}.

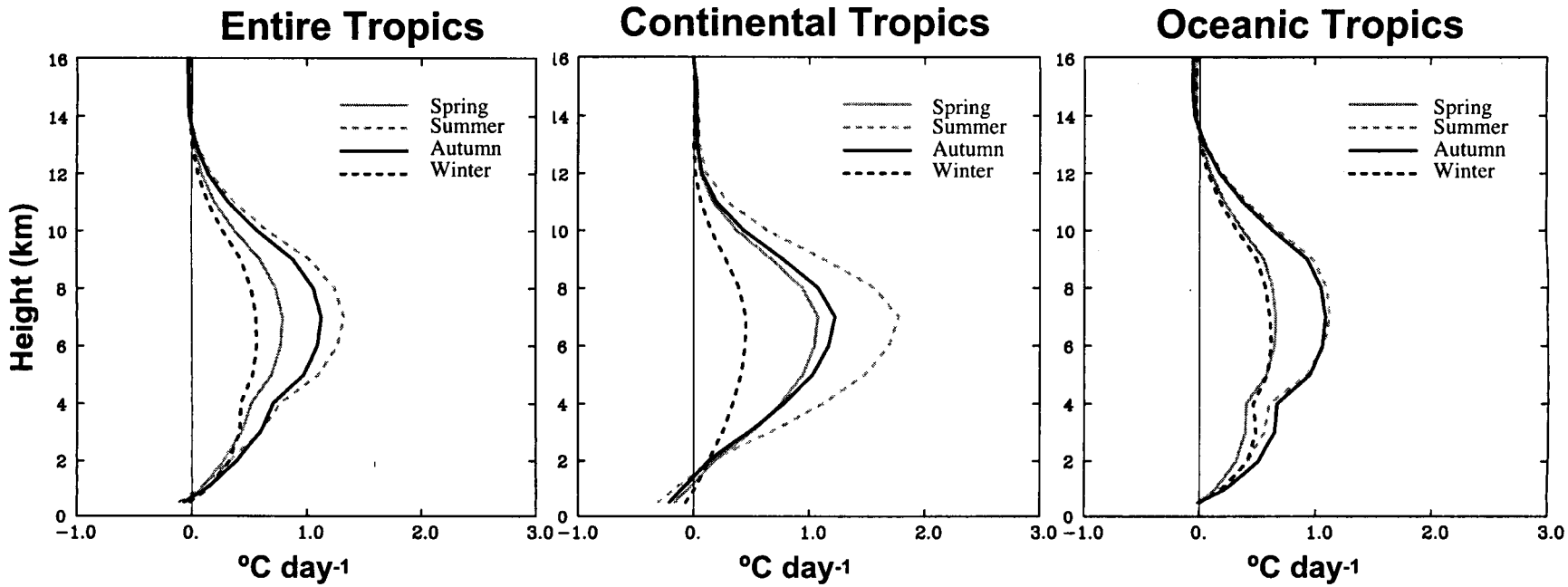

Figure 6: Five-year (1998-2002) mean Q_1 profiles estimated from CSH algorithm for spring, summer, autumn, and winter over entire tropics (left panel), continental tropics (middle panel), and oceanic tropics (right panel) -- all based on TRMM-PR retrievals.

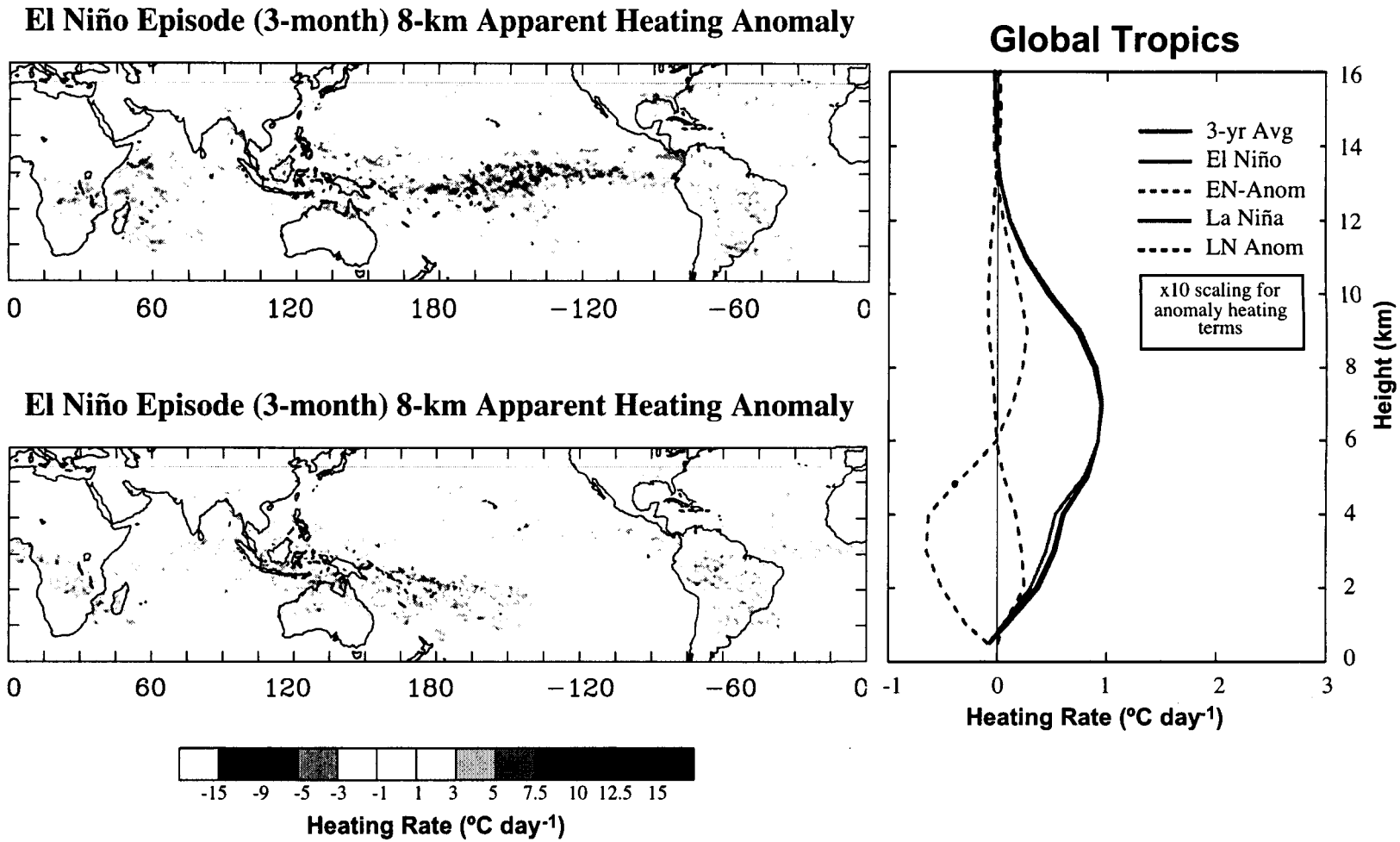

Figure 7: TRMM-PR-based Q_1 heating anomalies at 8 km AGL for La Niña episode during DJF 1997-98 (ULH panel) and El Niño episode during DJF 1998-99 (LLH panel) -- generated by CSH algorithm. Average 3-year (1997-99), 3-month El Niño episode, and 3-month La Niña episode heating and heating-anomaly profile pairs over entire tropics are shown in right-hand panel in black, red, and blue, respectively.

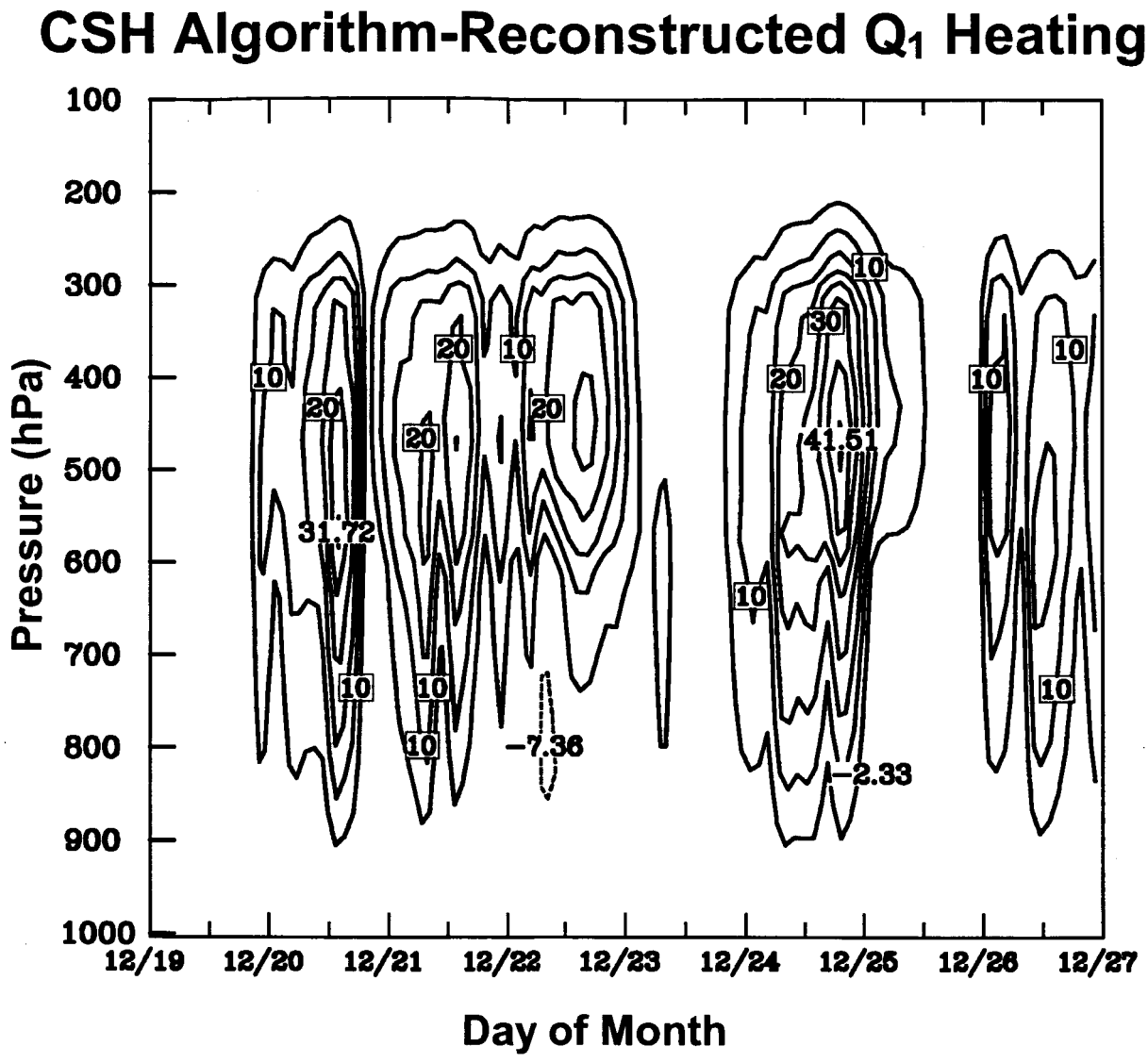

Figure 8: Evolution of $Q1$ profile reconstructed from GCE-CRM simulation by CSH algorithm averaged over TOGA-COARE IFA for 8-day period (19-27 December 1992) -- compare to results in Fig. 2. Reconstruction uses CRM parameters retrievable from PR data as input (i.e., surface rain rate and convective/stratiform fractions). [Contour interval is 5°C day^{-1}.]

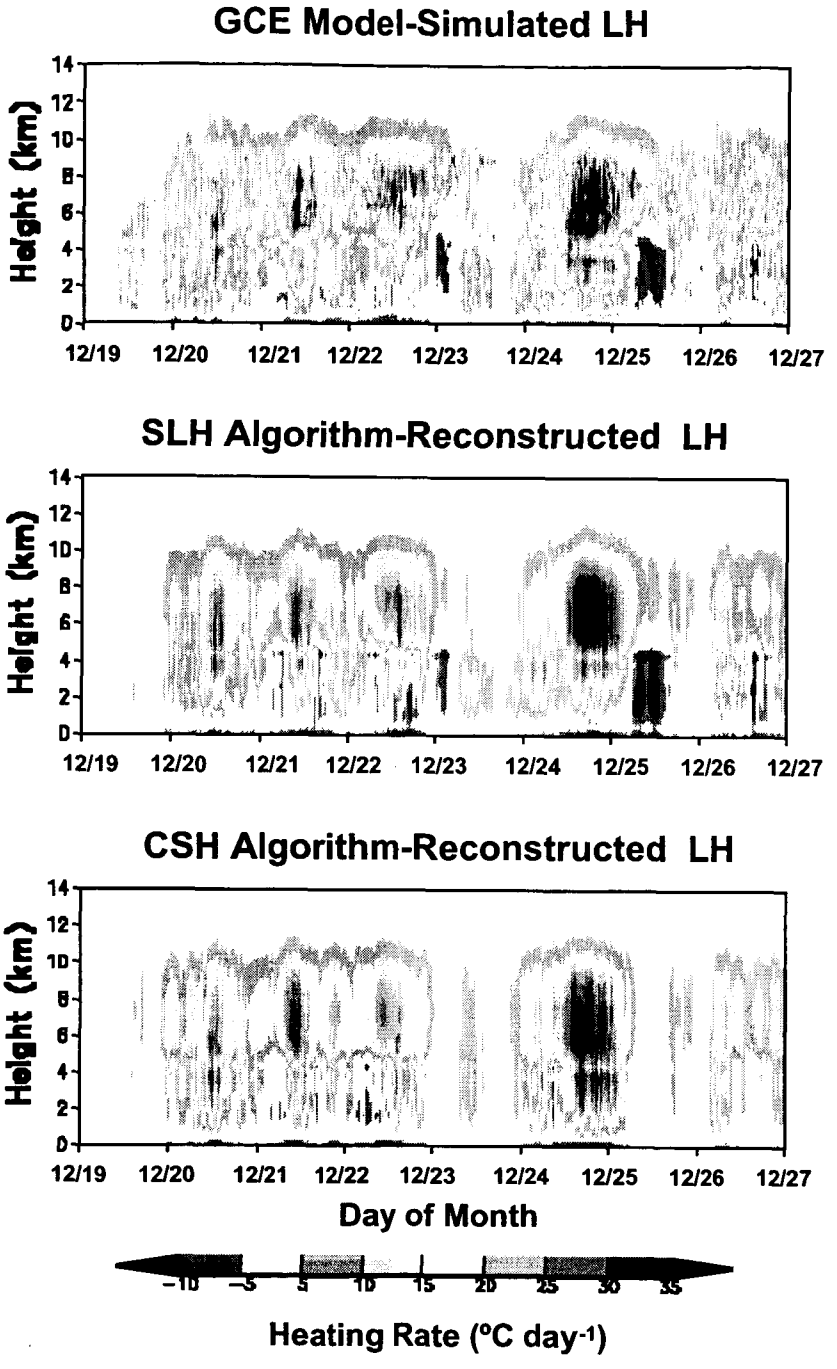

Figure 9: Evolution of LH profile (5-min time-step) from: GCE-CRM simulation (upper panel), SLH algorithm reconstruction (middle panel), and CSH algorithm reconstruction (lower panel), averaged over TOGA-COARE IFA for 8-day period (19-27 December 1992). Contour interval is 5°C day^{-1}. GCE-CRM simulated convective/shallow-stratiform/anvil stratus fractions, surface rain rates, PTHs, and melting level rain rates are used as inputs to SLH scheme with profiles averaged over 512 x 512 km grid mesh. [From Shige et al. 2004.]

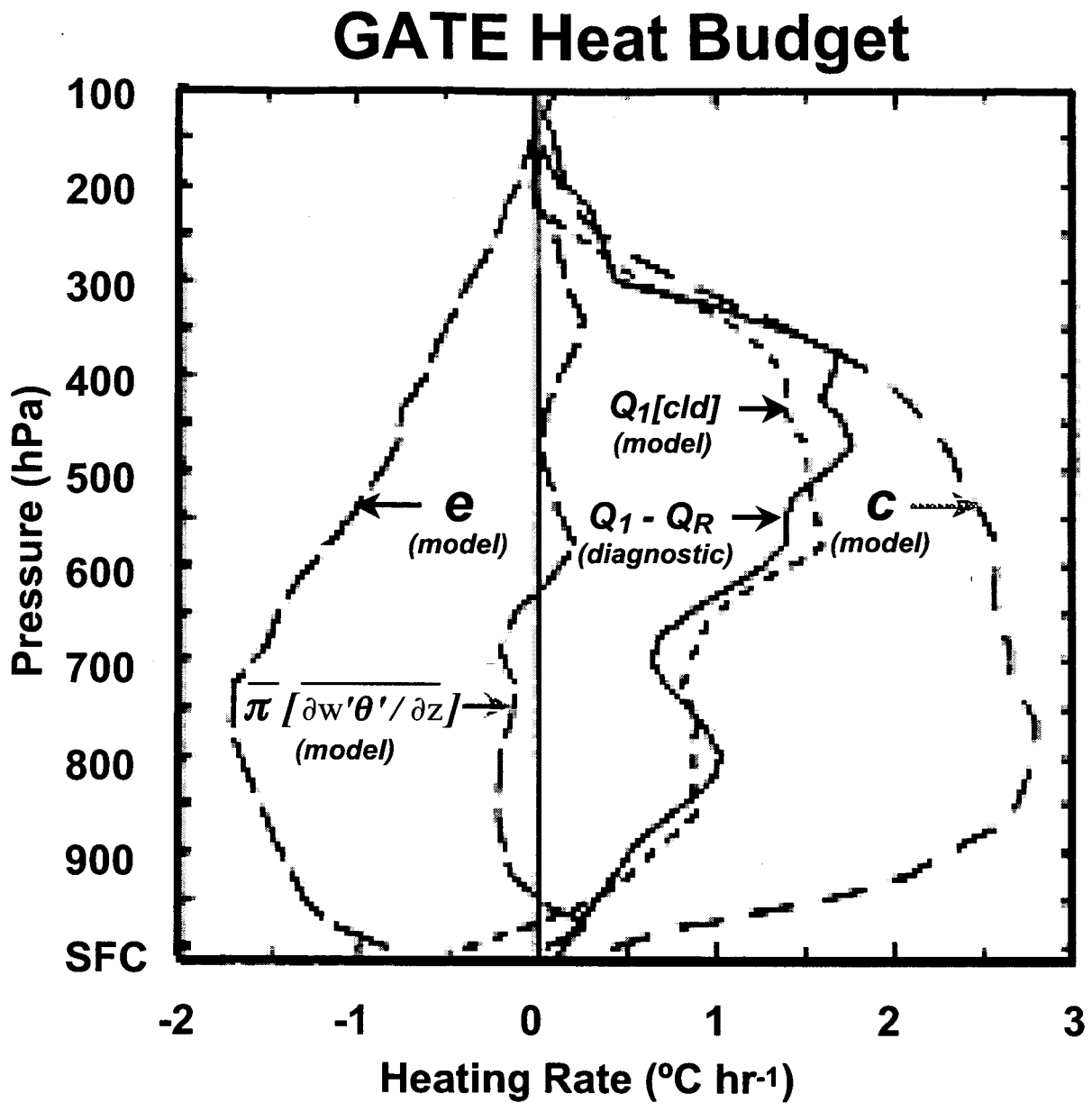

Figure 10: Cloud model simulation of GATE vertical profiles of heating rate by condensation (c), evaporation (e), vertical eddy heat flux convergence ($\overline{\pi}\,\overline{[\partial w'\theta'/\partial z]}$), and cloud partition of apparent heating ($Q_1[cld]$) -- along with diagnostic calculations of Q_1 - Q_R (using radiosonde data), all in units of °C hr^{-1}. [From Tao and Soong (1986).]

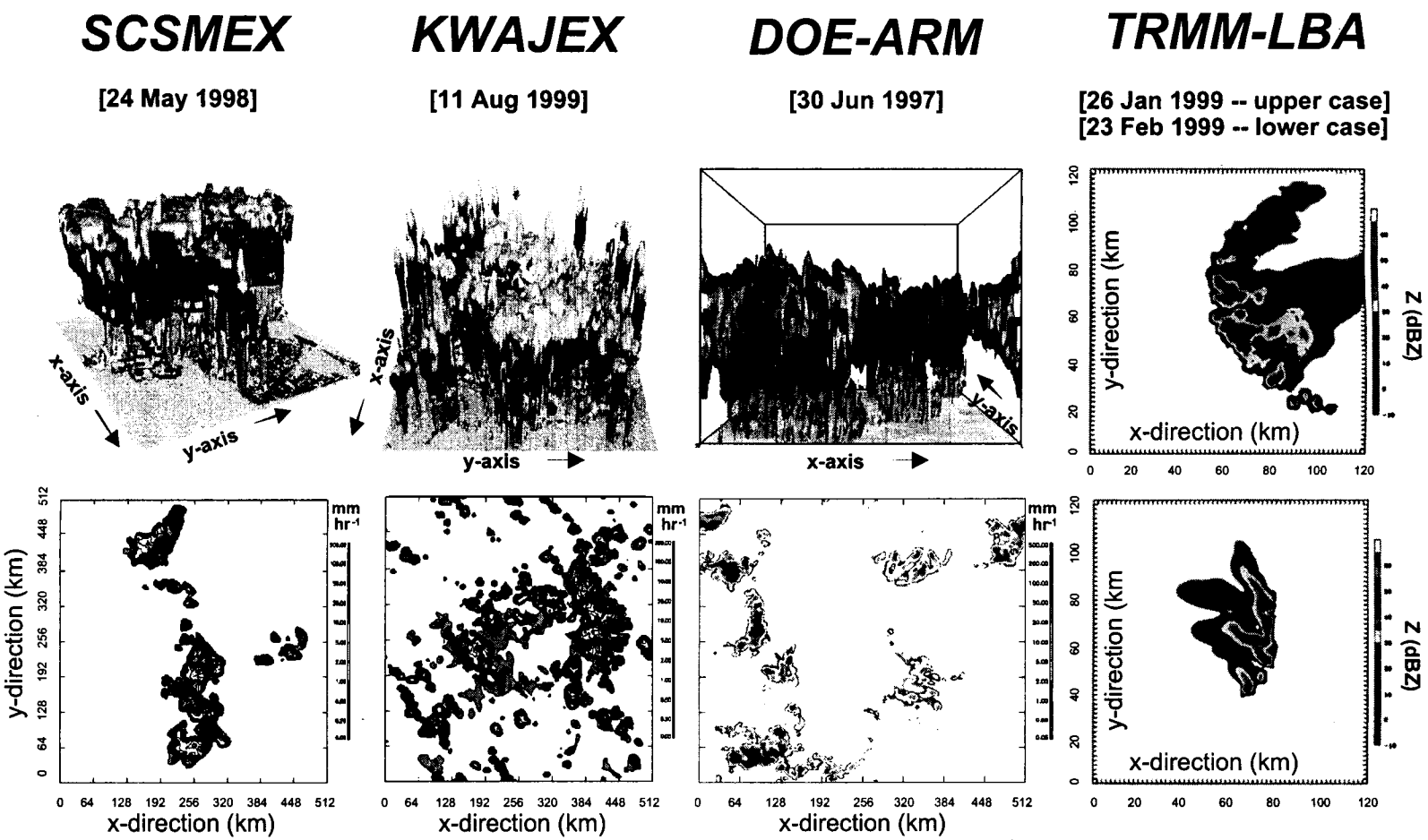

Figure 11: Three left-most pairs of diagrams illustrate isometric projections of volume hydrometeor distributions (upper panels) and plan-view surface rain rates (lower panels) for instantaneous realizations from GCE-CRM simulations of SCSMEX, KWAJEX, and DOE-ARM MCS storm cases. Upper panel iso-surface color scheme assigns white for cloud droplets and ice crystals, blue for snow, red for graupel and hail, and green for rain. Right-most pair of diagrams illustrate near-surface, forward-modeled radar reflectivities for TRMM-LBA easterly regime (upper panel) and westerly regime (lower panel) MCS cases, also based on GCE-CRM simulations.

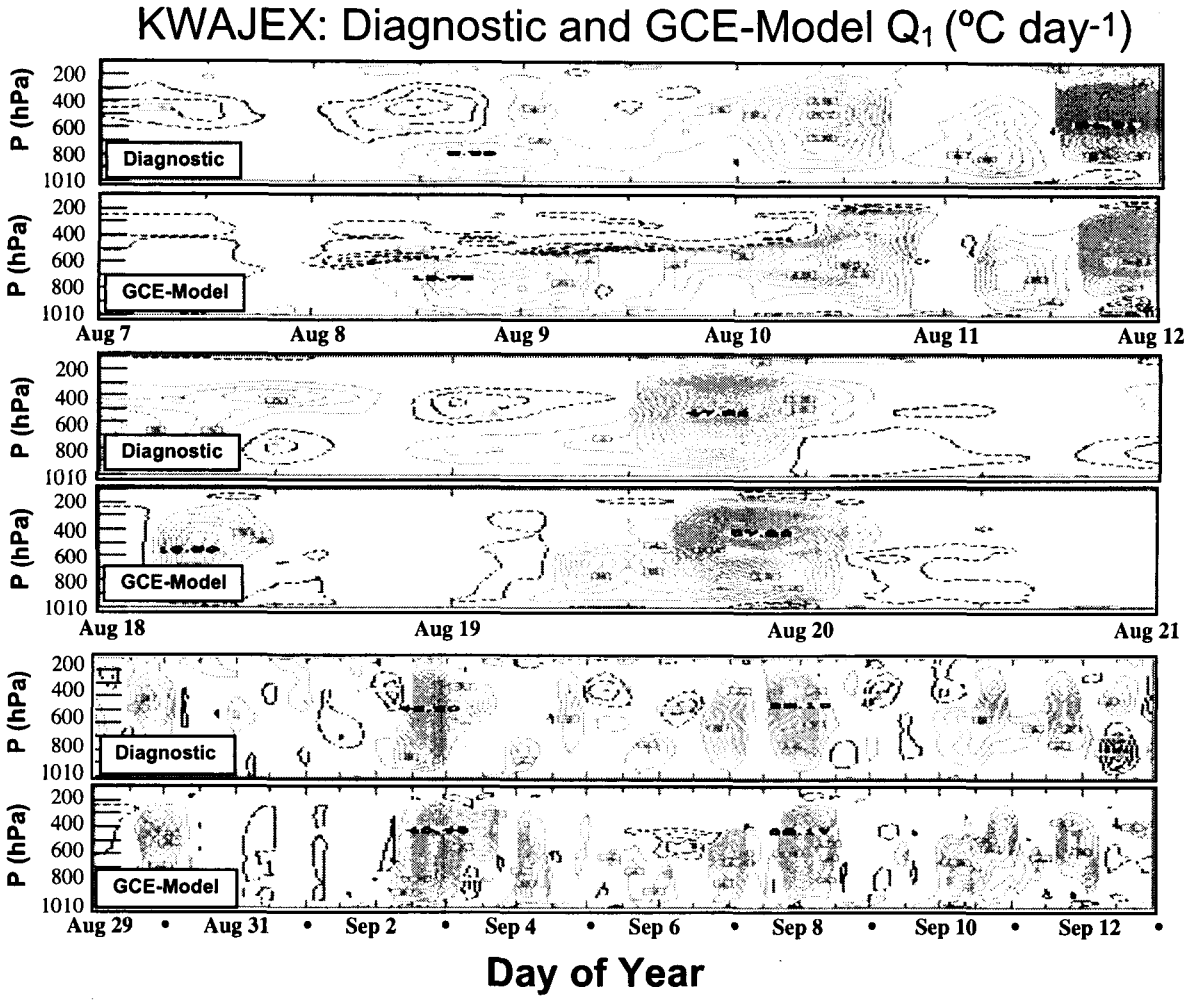

KWAJEX heat budget time series consisting of diagnostically-calculated and GCE-CRM-simulated $Q1$ profiles for three ıe sequences during IOP (upper, middle, lower panel pairs illustrate 5-, 3-, 15-day time series, respectively). Green urs indicate positive and negative $Q1$ regions, respectively.

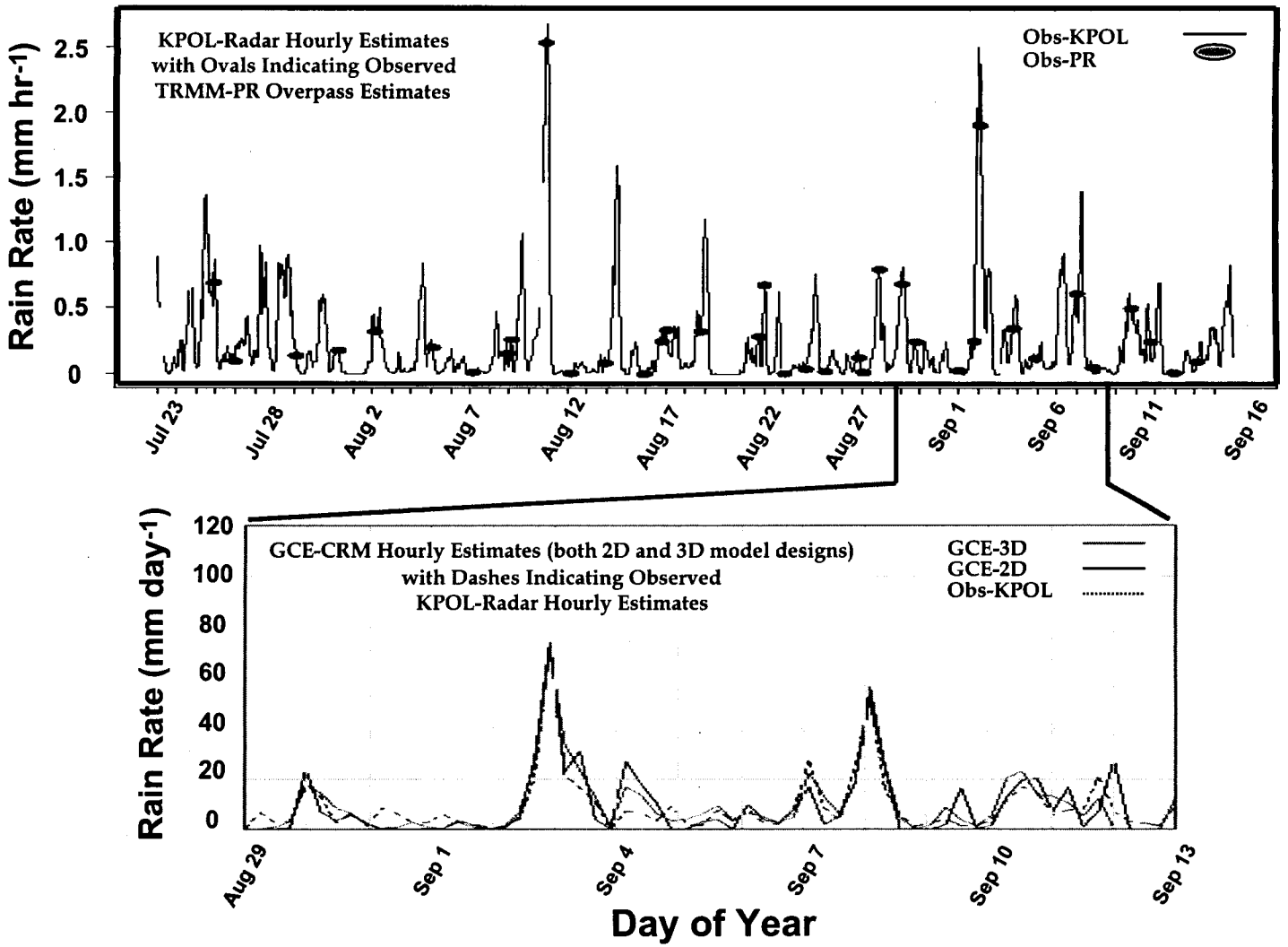

Figure 12a: KWAJEX rainfall time series consisting of measured and modeled rain rates. Both KPOL-Radar measurements and TRMM-PR retrievals are given for entire IOP, while GCE-CRM simulated estimates are provided from Aug 29 through Sep 12 (both 2D and 3D CRM designs are used to provide simulated rainfall). [Top diagram from Yuter et al. (2004).]

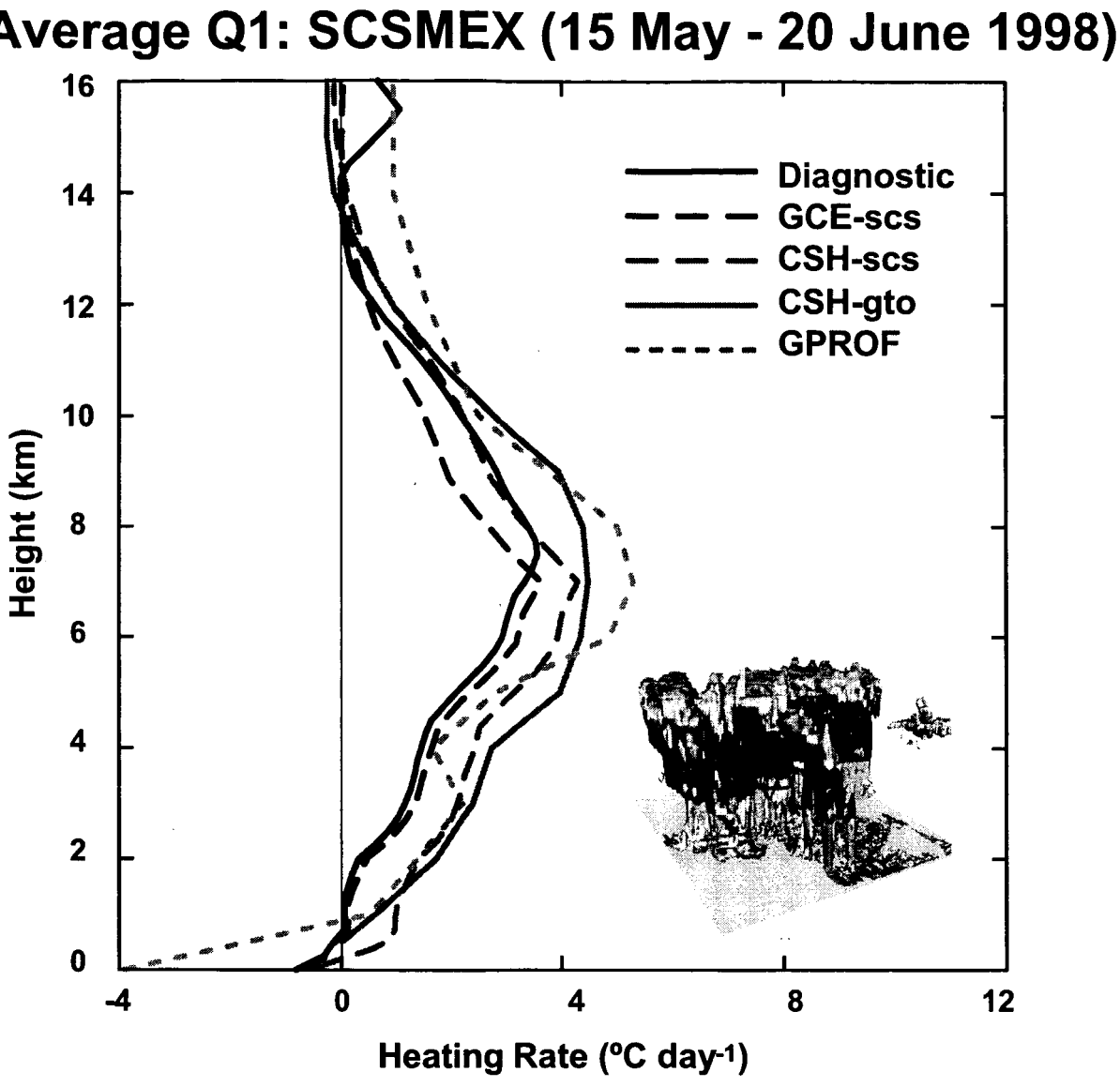

Figure 13: *Q1* profiles from diagnostic calculations (Johnson and Ciesielski 2002), GCE-CRM simulation, PR-based CSH algorithm, and TMI-based GPROF algorithm averaged over ~6 x 10 deg lat-lon box designated as SCSMEX-NESA for 37-day period (15 May - 20 June 1998). Two sets of look-up-table profiles are used with GCE-CRM and CSH algorithm representing conditions for: (1) South China Sea (scs), and (2) general tropical ocean (gto). Color insert is isometric rendition of GCE model simulation for 24 May 1998, where white, blue, red, and green iso-surfaces denote cloud droplets - ice crystals, snow, graupel - hail, and rain, respectively. [Most surface rainfall is produced by melting graupel.]

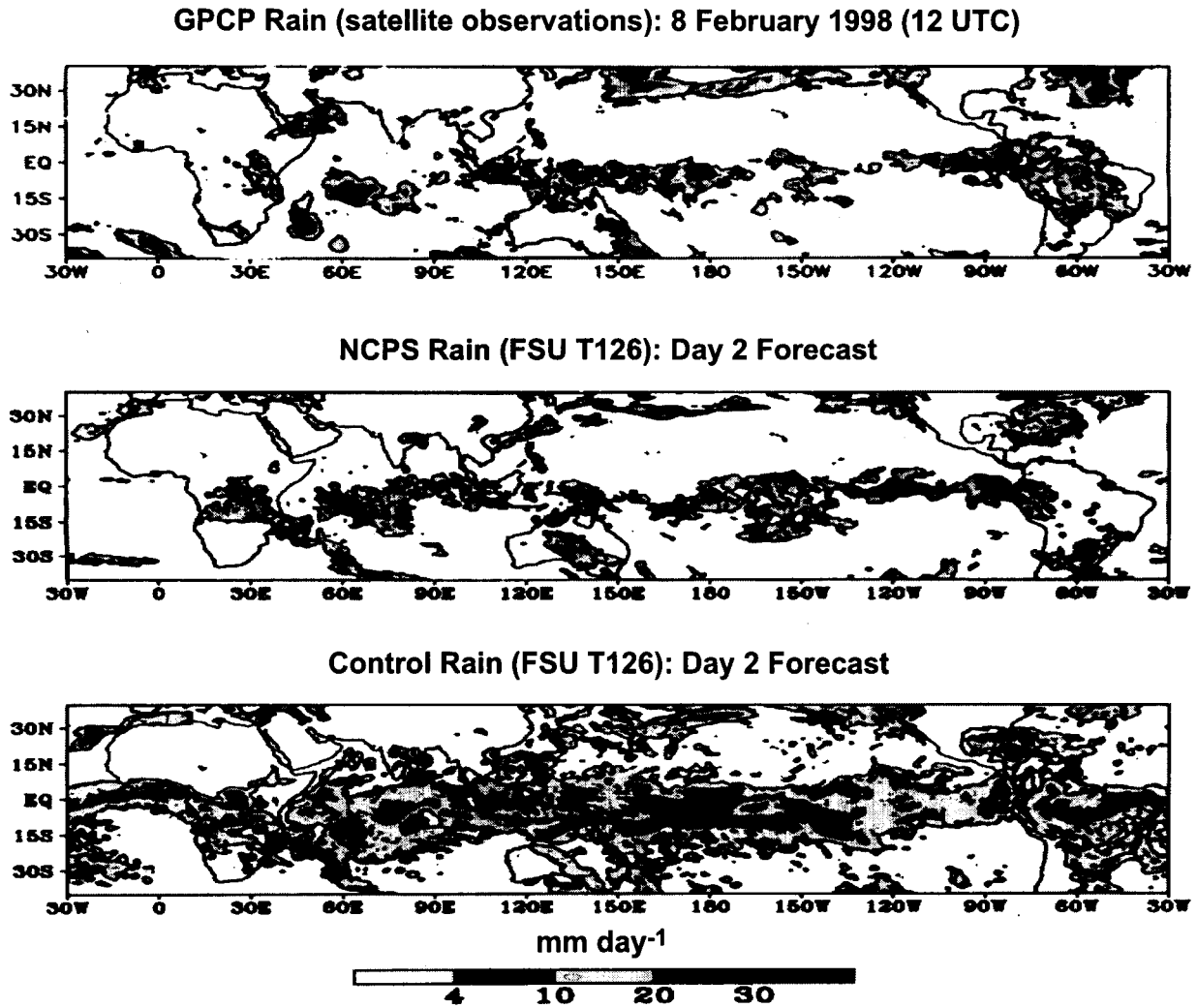

Figure 14: GPCP precipitation for 8 February 1998 representing blend of satellite retrievals and rain gauge observations (upper panel), Florida State University global spectral model (FSU-GSM) day-2 forecast from ECPS experiment (middle panel), and FSU-GSM day-2 forecast from control experiment (lower panel). [From Rajendran *et al.* 2004.]